Magnetisation of the IGM: Role of Starburst Dwarf Galaxies

Dissertation
zur
Erlangung des Doktorgrades (Dr. rer. nat.)
der
Mathematisch-Naturwissenschaftlichen Fakultät
der
Rheinischen Friedrich-Wilhelms-Universität Bonn

vorgelegt von
Amrita Purkayastha
aus
Kolkata, Indien

Bonn
September, 2013

Angefertigt mit Genehmigung der Mathematisch-Naturwissenschaftlichen Fakultät der
Rheinischen Friedrich-Wilhelms-Universität Bonn

1. Gutachter	Prof. Dr. Ulrich Klein
2. Gutachter	Priv. Doz. Dr. Dominik J. Bomans

Tag der Promotion:	28.11.2013
Erscheinungsjahr:	2014

"I would not know what the spirit
of a philosopher might wish more
to be than a good dancer."

- (Friedrich Nietzsche)

Contents

1 Introduction **17**

2 Observational Overview **21**
2.1 NGC 1569 21
2.2 NGC 4449 27
2.3 NGC 1569 & NGC 4449: comparison and relevance 30

3 Theoretical Background **31**
3.1 Synchrotron radiation 31
3.1.1 Total emitted power from a single electron 31
3.1.2 Power-law electron spectrum 32
3.1.3 Polarisation properties 33
3.2 Cosmic Ray Electron Dynamics 34
3.2.1 Energy loss processes for high-energy electrons 34
3.2.2 Diffusion-loss equation for high-energy electrons 36
3.3 Diagnostic Tools to Detect Magnetic fields in the ISM/IGM 38
3.3.1 Synchrotron emission 38
3.3.2 Faraday rotation 40

4 Observations and Data Reduction **43**
4.1 Observations with the WSRT at 92 cm 43
4.2 Data reduction method 44
4.3 Polarization calibration technique 46

5 Analysis and Results **47**
5.1 NGC 1569 47
5.1.1 Total intensity and morphology 47
5.1.2 Integrated radio continuum spectrum 48
5.1.3 Spectral index 49
5.1.4 Radial evolution of the break 50
5.1.5 Equipartition magnetic field strength 52
5.1.6 Spectral ages and wind velocity 52
5.1.7 RM synthesis 54
5.2 NGC 4449 55
5.2.1 Total intensity and morphology 55
5.2.2 Integrated radio continuum spectrum 56
5.2.3 Spectral index 56
5.2.4 Radial evolution of the break 56
5.2.5 Equipartition magnetic field strength 57

5.2.6 Spectral ages and wind velocity 57

6 Discussion, Conclusion & Future Prospects 63
6.1 Discussion 63
6.2 Conclusion 67
6.3 Future Perspective: LOFAR & SKA 68

A Error Analysis 71
A.1 NGC 1569 72
A.2 NGC 4449 77

Bibliography 88

List of Figures

1.1 Magnetic fields along the spiral arms of M51 . . . 18
1.2 Total intensity image of the Coma Cluster . . . 19

2.1 Multi-frequency view of NGC 1569 . . . 23
2.2 NGC 1569: Geometry of the disk and outflow . . . 24
2.3 Rotation measures in NGC 1569 . . . 26
2.4 Multi-frequency view of NGC 4449 . . . 29

3.1 Function describing the total power spectrum of synchrotron emission . . . 32
3.2 Velocity cone of an ultra-relativistic electron . . . 33
3.3 Spectral ageing . . . 38
3.4 Minimum energy plot as a function of magnetic field . . . 39
3.5 Polarization rotation due to the Faraday effect . . . 40

4.1 UV coverage of NGC 1569 . . . 44

5.1 NGC 1569: Total power map . . . 47
5.2 NGC 1569: Integrated radio continuum spectrum . . . 49
5.3 NGC 1569: Spectral index map . . . 50
5.4 NGC 1569: Radial evolution of the break frequency . . . 51
5.5 NGC 1569: Break frequency Vs radius . . . 51
5.6 NGC 1569: Equipartition magnetic field strength . . . 53
5.7 NGC 1569: Spectral Age Vs Radius . . . 54
5.8 NGC 4449: Total power map . . . 55
5.9 NGC 4449: Integrated radio continuum spectrum . . . 57
5.10 NGC 4449: Spectral index map . . . 58
5.11 NGC 4449: Radial evolution of the break frequency . . . 59
5.12 NGC 4449: Break frequency Vs radius . . . 59
5.13 NGC 4449: Equipartition magnetic field strength . . . 60
5.14 NGC 4449: Spectral Age Vs Radius . . . 61

6.1 Radial intensity distribution of NGC 1569 and NGC 4449 . . . 63
6.2 Spectra of the “extra” flux in NGC 4449 . . . 64
6.3 Schematic overview of magnetic field build-up during galaxy formation . . . 66
6.4 Simulated magnetic fields in dwarf galaxies . . . 67
6.5 The Future: LOFAR and SKA . . . 69

List of Tables

2.1 Properties of NGC 1569 and NGC 4449 21

4.1 Summary of WSRT 92 cm Observations 45

5.1 NGC 1569: Integrated flux densities at different radio frequencies 48
5.2 NGC 1569: Results at a glance 54
5.3 NGC 4449: Integrated flux densities at different radio frequencies 56
5.4 NGC 4449: Results at a glance 61

A.1 NGC 1569 at λ92 cm: RMS and Mean 72
A.2 NGC 1569 at λ92 cm: Radially averaged intensities 72
A.3 NGC 1569 at λ20 cm: RMS and Mean 73
A.4 NGC 1569 at λ20 cm: Radially averaged intensities 73
A.5 NGC 1569 at λ13 cm: RMS and Mean 74
A.6 NGC 1569 at λ13 cm: Radially averaged intensities 74
A.7 NGC 1569 at λ6 cm: RMS and Mean 75
A.8 NGC 1569 at λ6 cm: Radially averaged intensities 75
A.9 NGC 1569 at λ3 cm: RMS and Mean 76
A.10 NGC 1569 at λ3 cm: Radially averaged intensities 76
A.11 NGC 4449 at λ92 cm: RMS and Mean 77
A.12 NGC 4449 at λ92 cm: Radially averaged intensities 77
A.13 NGC 4449 at λ49 cm: RMS and Mean 78
A.14 NGC 4449 at λ49 cm: Radially averaged intensities 78
A.15 NGC 4449 at λ20 cm: RMS and Mean 79
A.16 NGC 4449 at λ20 cm: Radially averaged intensities 79
A.17 NGC 4449 at λ6 cm: RMS and Mean 80
A.18 NGC 4449 at λ6 cm: Radially averaged intensities 80
A.19 NGC 4449 at λ3 cm: RMS and Mean 81
A.20 NGC 4449 at λ3 cm: Radially averaged intensities 81

Acknowledgements

I am an emotional fool who works with her heart. It has been very difficult (and understandably so) for some people to fathom why on earth I would want to take some time to write this acknowledgement. But you see, my heart went into it! And like with all matters of the heart, it takes time. No PhD can be done alone. So, here it is, my utmost sincere words of gratitude to every single soul who has touched my heart over the last three years of my PhD.

Needless to say, it has been quite the journey, like it is for everyone who has chosen to walk this path. I probably went about it the wrong way, having unrealistic expectations from myself (and others at times), taking all of it way too seriously, losing the big picture and forgetting for a while that life is far greater than this. My whole fascination for this field was based on my awareness of the sheer insignificance of anything earthly in the context of the whole Universe. The infinity of Space beckoned me very early in life, and I found an alluring comfort in the knowledge of our own insignificance. Someone should have advised me to study Philosophy, but Physics was the natural biased choice, coming from a professor's daughter. So here I was, and life became very uncomfortable as the bubble of my philosophical fascination burst, plunging me headlong into depression everytime some method didn't work and the results looked hopeless. Yes, for a while I became way too obsessed with my problems, I lost perspective. Anyway, let me save the rest of that boring story for my boring autobiography. This acknowledgment is not about me, it's about you. In the following lines, you will find yourself somewhere. I am sorry I couldn't think of any particular order to arrange your names. Well, you just have to read the whole darn thing!

First of all, I would like to thank Dr. Rainer Beck for spotting my application among a pile of rejected IMPRS applicants, probably seeing some potential in it and forwarding it to Uli. It was really for him that I was here in the first place. Over the following three years, I found a willing mentor in Rainer, who readily pointed out a glimmer of light whenever I was tired of swimming in the darkness. Especially in the last few months, when the results were finally coming in, he had been available for discussions whenever I asked. Thank you, Rainer.

I am grateful to Prof. Dr. Uli Klein above all for giving me the PhD offer. Reading his acceptance email had been one of those cherished, jubilant moments of my life. I still remember that first day when he picked me up from Bonn Hauptbahnhof and drove me to the Max Planck guest house. Since it was Sunday, he had pre-arranged for food to be stored in the refrigerator. That was so thoughtful of him. I thank him also for never saying "no", be it for work-related travel, or leaves, or visa extension, or even squeezing in my thesis defence on short notice in his busy schedule. Thank you, Uli.

I thank Dr. Dominik Bomans for being so friendly and welcoming during my visit to Bochum. He was one of the few people during that difficult time whose patient ears and considerate words helped me stay afloat. I only wish there were more time and

opportunity to work with him.

My heartfelt thanks go out to Ms. Elisabeth Kramer for always being her friendly, smiling, polite self, all through these three years. She was the point of contact between me and all German authorities, especially in the first year of my stay, and that of course made her indispensable to me! Thank you, Elisabeth, for the little presents you left at my desk on so many occasions, which always warmed my heart.

I thank Ms. Christina Stein-Schmitz for all the little help she provided me all through. When no one else knew, ask Christina! That's how it really went with administrative queries. She was the only person who greeted me by my first name *everytime* I ran into her in the corridor. People forget what a difference such small things can make!

This research was conducted in the framework of the DFG Forschergruppe 1254 Magnetisation of Interstellar and Intergalactic Media: The Prospects of Low-Frequency Radio Observations.

I thank Prof. Dr. Michael Kramer for so generously supporting me financially for the last two months of my PhD. Along with him, I thank Ms. Tuyet-Le Tran and Ms. Margret Bernhardt for efficiently taking care of all the bureaucracy during those two months.

Sincere thanks to Andreas Bödewig and Dr. Reinhold Schaaf for all the computer-related help they have provided all through.

I am grateful to Nadya Ben Bekhti for many reasons - for being the sunshine of the institute, for the coffee breaks, for the badminton games, for the parties and the dancing and for all the fun evenings at conferences. Most importantly, for listening and understanding my problems at work and helping me overcome them in the best way she could. Thank you, Nadya dear.

I thank Shahram Faridani and Lars Flöer, for being such helpful officemates.

Thank you Dr. Marita Krause, David Mulcahy, René Gießübel and Andreas Horneffer for the helpful discussions.

Thanks are due to Björn Adebahr, Carlos Sotomayor and Dr. Enno Middelberg for all the time they generously gave me during my visits to Bochum.

Now I come to that section, where my heart falls short of words. I will try though.

Monica Trasatti, my Italian bella, what would I have done without you! Our journey in Bonn started together and we both have seen each other through times that possibly nobody else did. Our friendship grew rapidly and then went through fire for a while. But still here we are at the end of this journey, still going strong! There have been days when the only reason I came to work was seeing you. Thank you for your love, tolerance and reassuring presence all through.

Disha Varma, another invaluable girlfriend for life I have made here. Without her many, many dark days would not have ended with raucous laughter over home-cooked food and wine. She has been there when nobody else had the time or the energy, and she probably had the biggest excuse of all. That's Disha, the most loyal friend ever! She also happens to be the best dance partner I have ever had. I love you forever, Dish.

Sheetal Saxena, thank you for your love, trust, confidence and loyalty. You are one of the strongest women I know.

Sambaran Banerjee, the first friend I had made here, and the most helpful of all. Thanks for making those first few weeks in Bonn easier for me, for all the yummy cooking experiments and for your loyal friendship.

Emiliano Orlandi and Lorenzo Lovisari, two of the nicest guys I met here, have been a constant. Thank you for so many good times, lovely dinners, crazy parties, wild dancing - I will miss all that.

Manusmriti Singh, Sameera Salim and Roopika Menon - my girlies, thanks for being there throughout. You had been part of my tiny support system here in this foreign land, in a way that felt like home.

Carolina Mora, my sweet friend and jogging partner, we made rounds around the fields behind the institute on so many summer evenings. You motivated me, thank you!

Felipe Alves and Anna Laura Rezende, the most beautiful couple of all, thanks for all the happy times. Felipe, thanks for lifting my mood on those days at work when nothing worked!

Hananeh Saghiha, Matthias Klein, Aarti Nagarajan, Bharadwaj Vijaysarathy, Sutirtha Sengupta, Jennifer Pollack and Debashis Sanyal, thank you for all those evenings of food, drinks and fun. Behnam Javanmardi, thank you for the music!

Somehow learning German became my most important hobby in the last three years. I thank Katharina Schlieper for being the best German teacher I have ever had! Those evenings at IFS filled up a big part of the emptiness within.

Sandra Gröger and Martin of the International Choir Uni Bonn, for the lovely Monday evenings at the choir practice. Being associated with music, even in this one small way, kept me going.

In the middle, along came a "storm" and a "stranger". I thank both, for enriching my life, even for all the pain and suffering that followed, which made me grow and understand myself better.

Kiron Doulah for being such a kind friend, and initially the only one in my dorm who extended a hand of friendship. Thanks for being there, it meant a lot to me.

Fabian Schwartzkopff for being so nice to me at such a difficult time of my life. You did more for me than you would ever know.

Isabel Busch, my study-buddy, thanks for the few evenings we spent together talking about English literature, the passion that we share.

Dr. DRL, thank you from the bottom of my heart for listening to me, understanding me and helping me understand. Without your expert contribution, the last year would have been very different.

Susmita Chakravorty for making the last few months in Bonn so colourful, and Ritam Roy, my tiny Utpotang, for evoking a fountain of love in my heart with his innocent presence.

Deepa Reddy, our paths crossed luckily on that first trip to Germany. That starry-eyed, ambitious girl told you all about her dreams. I am so happy we met that day, and I am so happy that I get to thank you today, when one of those dreams has been achieved. You inspired me, and will continue to do so.

Thanks to Sagnik Sinha for his unconditional love and support and to Dipan Sengupta for being always a friend in need and for being my 'bishupagol'.

Bodhisatwa Sadhu and Tania Roy for always caring about me, despite living oceans apart. Talking to you always made the PhD seem less painful!

Coming now to that section of people here, thanking whom is actually hilarious, because no word of thanks would suffice. Probably thanks are unnecessary, but I still need to.

Rahul Singh, thank you for being that positive force in my life that is the strongest and the most reliable.

Tina Ganguly, thank you for having the strongest belief in my potential. Nobody else loves me so blindly I think. Thanks, my Angel, for the endless love.

Jhelum Podder, it's been 26 years of "us". You have literally always been there, and that we know will never change. Thanks darling for always being on my side.

Mathew Abraham Antony, I will try to write this without crying I promise! We both shared the same dream when life brought us together - the dream of pursuing higher-studies abroad. We worked on that dream together. You have been a part of this dream in a way noone else has and today, when this PhD is done, I am sure you would be happy for me in a way noone else can be. Thank you, Mat, for being such a significant part of my dream.

Nirupam Roy, you have no idea what you have done for me. Probably it is best that way! I just want to thank you for being my *de facto* supervisor, my mentor, my friend, my brother all at once. Thank you for all the care, all the fun, all the laughter and for just being your stupendously crazy self.

Julius Donnert, let me not say much here, I have my whole life ahead to say all that I want to. Let me just say, without you it really, really wouldn't have been possible. You are my strength. Had I believed in God, this would have been the time to thank him as well, for giving me you.

Corinna Lüdicke and Bertold Donnert, thank you for having such open hearts, for your unconditional love and care and for spoiling me like crazy! You have given me something very precious - a feeling of being truly accepted in this country.

Vandana Alase Hazra, thank you for always being my real teacher, my Guru. For me, Dance is what it is because of you. I consider myself very lucky!

Chandrani Roy Kachari (Chhordibhai), thank you for being my hero, my inspiration, my confidante, my friend, my sister. I am so thankful to have you in my life.

Gitanjali Purkayastha (Ma), your quiet strength and deep wisdom continue to amaze me. I don't know anybody else with such a great capacity to love. There had been so many times in the last three years when I called you up because I felt miserable, and just the sound of your voice was enough to make me feel better. I love you, Ma.

Prof. Dr. R.D. Purkayastha (Baba), I really owe it to you for instilling me with strength, perseverance and ambition. No wonder I followed in your footsteps.

Thank you, Anirban Purkayastha (Dada) and Debdutta Paul (Debbie), for all the support and love.

This is not the end, my friend. I have lightyears to go still, there are dreams to fulfill, there are promises to keep, not much time to sleep! I move on from here along with a treasure chest of fond memories, hard-learned lessons and a few friends for life. A new story begins now. And the only thing I know for sure is that I will continue to be an emotional fool who works with her heart.

Abstract

Magnetic fields are ubiquitous in the Cosmos. They are observed on all scales – from our solar system to galaxy clusters millions of light years away. The dynamo theory and the theory of gravitational compression during structure formation in the early Universe explain how magnetic fields are generated. However, magnetohydrodynamic equations tell us that both these mechanisms require the presence of an initial seed field, which is then amplified. The origin of this seed field remains unclear. It could be either primordial, or it could have been generated during structure formation. For the latter case, one of the possibilities suggested by theory and tested by simulations is that the magnetic seed fields could have been generated in the very first stars, and then in the process of galactic evolution, amplified and driven out by galactic winds into the inter-galactic medium (IGM). According to the standard ΛCDM cosmological model, low-mass dwarf galaxies were large in number in the early Universe. Hence, it is possible that they could have played an important role in magnetising the IGM by this process.

Low-frequency radio observation is one of the ways to find observational evidence for this theory, because synchrotron emission from cosmic sources, which is most easily detectable at low radio frequencies, is a tracer of total magnetic field strengths. Also, the Faraday effect, that is very significant at low frequencies, can be a diagnostic tool to detect weak magnetic fields. With this motivation, we observed two nearby star-forming dwarf galaxies NGC 1569 and NGC 4449 at a low frequency of 350 MHz, with the Westerbork Synthesis Radio Telescope, in full polarisation.

We detect radio continuum emission from both galaxies and find that the extent of the synchrotron halo of NGC 1569 is larger than that found in all higher radio frequencies. When analysed using complementary images at higher frequencies, the spectra in the core of both galaxies are found to be very flat (~ -0.4), which might point towards non-linear diffusive shock-acceleration. The break in the spectra of both migrates towards lower frequencies with time. The equipartition magnetic field strength in both the halos reaches down to $\approx 4\,\mu$G, which is comparable to that predicted by simulations. We estimate the spectral ages of both the galaxies and find high wind velocities in both, which shows that winds from these galaxies can indeed drag magnetic fields and cosmic-ray electrons into the IGM. Rotation measure synthesis performed on NGC 1569 was unable to detect polarised emission.

We conclude that our observational investigation gives reasonable evidence that starburst dwarfs may have played an important role in magnetising the IGM. The detection of IGM-scale magnetic fields and of weak polarised emission from dwarf galaxies are most probably limited by telescope sensitivity. Observations at even lower frequencies with new telescopes like LOFAR (or SKA in the near future), which will have far higher sensitivity, should be able to detect larger synchrotron halos and consequently better constrain the role of starburst dwarf galaxies in magnetising the IGM.

Chapter 1

Introduction

Magnetic fields have been observed in the Universe on all astrophysical scales – in stars (Donati & Landstreet, 2009), in molecular clouds (Heiles & Crutcher, 2005), in the Galaxy (Reich & Reich, 1986; Gaensler et al., 2001; Han et al., 2006), in nearby galaxies (Beck & Hoernes, 1996; Fletcher et al., 2011; Adebahr et al., 2013), in active galactic nuclei (AGNs; de Gasperin et al. 2012) and in galaxy clusters (Willson, 1970; Giovannini et al., 2009; Brown & Rudnick, 2011). Furthermore, Dolag et al. (2011) proposed a lower limit on the strength and filling factor of magnetic fields in voids of the Large Scale Structure. Fig. 1.1 shows the magnetic fields in the spiral arms of the galaxy M51 and Fig. 1.2 shows the observed radio halo and relic in the Coma cluster (a direct indication of the presence of magnetic fields).

It is a well-accepted theory that these magnetic fields are produced by amplification of pre-existing weaker magnetic fields via different types of *dynamos* (Widrow, 2002; Brandenburg & Subramanian, 2005; Beck et al., 2012) or via gravitational compression during structure formation. Structure formation refers to the standard cosmological model which tells us that structures in the Universe formed in a "bottom-up" hierarchical manner, wherein small dark matter halos formed first and subsequently merged to form larger structures (Press & Schechter, 1974; Sheth et al., 2001). This process was driven by gravitation in the matter-dominated era of cosmic evolution. Gas cooled in the gravitational potential of the dark matter to form the first over-dense structures like population III stars and protogalaxies. As the structures merged, galaxies and eventually galaxy clusters formed.

Both the mechanisms to amplify magnetic fields (mentioned above) require the presence of an initial "seed" field. This is because the dynamics of astrophysical plasmas are governed by *magnetohydrodynamics* (MHD), and its induction equation does not have a *source* term. The origin of this seed field is a long-standing question (Kulsrud & Zweibel, 2008; Widrow et al., 2012; Durrer & Neronov, 2013). The existing data on magnetic fields in galaxies and galaxy clusters can not provide direct constraints on the properties and origin of the seed fields.

There are two broad classes of theories to explain the origin of cosmic magnetic seed fields. One hypothesis is that the seed fields are *primordial*, i.e., they are relics of the early Universe, and have been present before any structure formation took place (Piddington, 1964, 1972; Howard & Kulsrud, 1997; Battaner & Lesch, 2000). The other possibility is that these seeds were generated during structure formation and processes comprising galactic evolution, and then amplified and subsequently spilled out along with outflows into the galaxy or inter-galactic space (Widrow 2002, and references therein). The second

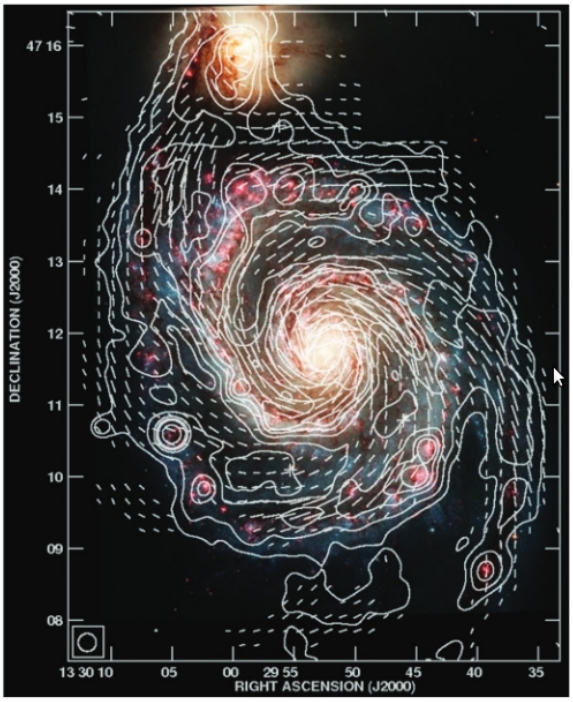

Fig. 1.1: $\lambda 6$ cm radio emission from M51 at 15 arcsec resolution from VLA and Effelsberg observations, overlaid on a Hubble Space Telescope optical image. Also shown are the magnetic field vectors of polarised emission (Fletcher et al., 2011).

possibility can, in turn, be divided into two processes:

1. Magnetic fields can be seeded in AGNs of large elliptical galaxies or quasars and then transported to the IGM via powerful relativistic jets and radio lobes associated with them (Rees, 1987; Chakrabarti et al., 1994; Xu et al., 2010; de Gasperin et al., 2012), or

2. Magnetic fields can be seeded during the process of star-formation and evolution in protogalaxies and then transported into the IGM by galactic "winds".

In the context of case (2) above, Kronberg et al. (1999) was the first to propose that *dwarf* galaxies, formed at or before redshift ~ 10 (i.e., when the Universe was 0.48 Gyr old) in a bottom-up hierarchical merging scenario, can effectively seed the IGM by the present epoch. The two prime arguments for dwarf galaxies as agents of magnetisation are:

i. their large number in the early universe as predicted by the hierarchical structure formation theory, and

ii. their low mass implying shallow gravitational potentials and low escape velocities, which render the outfow of winds carrying magnetised gas and relativistic particles easily feasible.

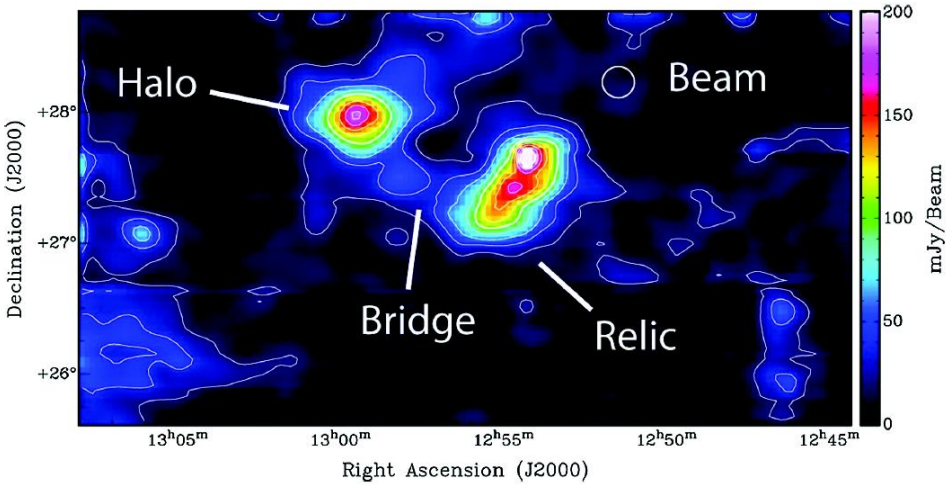

Fig. 1.2: GBT total intensity image of the Coma Cluster at 1.41 GHz (Brown & Rudnick, 2011).

The transport of the magnetic fields to the IGM by galactic winds were studied further by Bertone et al. (2006). They used a semi-analytic model for magnetised galactic winds coupled to high-resolution N-body simulations of structure formation and found that galactic winds are able to magnetise a substantial fraction of the cosmic volume. Later, Donnert et al. (2009) and Dubois & Teyssier (2010) numerically modelled the supernovae-driven winds in dwarf galaxies. Their simulations provided an understanding of the origin of IGM magnetic field at a level of 10^{-4} μ-Gauss. In a most recent study, Beck et al. (2013a) presented a first numerical model for the supernova-seeding and evolution of magnetic fields in protogalaxies. In the light of all these studies, the motivation to find observational evidence that dwarf galaxies can magnetise the IGM is clear.

Observational signature of total magnetic field strengths comes from a specific astrophysical radiation mechanism called *synchrotron* emission (Ginzburg & Syrovatskii, 1965). This radiation occurs when relativistic electrons (Lorentz factor, $\gamma \approx 10^4$), referred to as *cosmic ray electrons*, gyrate in a magnetic field, and it is most easily detectable at radio wavelengths. In fact, the rapid growth of the field of radio astronomy in the past few decades is a direct consequence of the fact that cosmic objects of all scales emit intense radio waves through the process of synchrotron emission. Rapid advancement in technology of telescopes allowed the detection of synchrotron emission from various sources, including dwarf galaxies. The first detection of a radio synchrotron *halo* around a dwarf galaxy was by Klein et al. (1996) in NGC 4449. Independent observations of gas kinematics with slit spectroscopy and X-ray measurements of gas temperature in dwarf galaxies have also shown that dwarfs have strong winds that can drive metals and hot gas out of the galaxy disk (della Ceca et al., 1996; Martin, 1998, 1999). Further low-frequency radio studies have found large synchrotron halos and magnetic fields being dragged out of the galaxy by strong winds (Mühle et al., 2003; Lisenfeld et al., 2004; Chyży et al., 2000; Kepley et al., 2010). These studies have detected synchrotron halos of the order of a few kiloparsecs and magnetic fields of the order of a few μ-Gauss out into the halo. In order to find nano-Gauss level magnetic field strengths, which is the

IGM magnetic field that is predicted by simulations, we need to be able to detect larger synchrotron halos ($\geq$ 50 kiloparsecs), and this can only be achieved by better telescopes of higher resolution and sensitivity at lower meter-wavelengths.

The advent of new-age, state-of-the-art telescopes like LOFAR[1] and SKA[2] will now make this possible. In fact, these telescopes and their pathfinders have ushered in a golden era of the field of *Low Frequency Radio Astronomy*. Observation of the *Cosmic Web* may now become possible, which will open up a new window into the structure of the Universe larger than superclusters, e.g. filaments and voids. This project on the role of dwarf galaxies in magnetising the IGM was motivated and designed at the time LOFAR was being commissioned, and we had intended to use LOFAR data of dwarf galaxies to aid our investigation. As discussed, LOFAR promises to detect weak synchrotron emission out to larger distances than ever before. LOFAR will also measure the *Faraday effect*, which is the rotation of polarization plane of low-frequency radio waves, and gives another tool to detect weak magnetic fields. However, LOFAR took longer than expected to be commissioned and has started delivering science data only this year. Hence, for this project, we decided instead to work with low-frequency data from the Westerbork Synthesis Radio Telescope (WSRT).

Our observations at 350 MHz (92 cm) of two dwarf galaxies with the WSRT is the first time dwarf galaxies are observed at this wavelength, and hence provide an important bridge between future LOFAR observations and existing higher frequency observations. Our primary goal is to find the synchrotron halos around these galaxies and find the magnetic field strengths out into the halo. Additionally, we estimate the age of the relativistic particles and velocity of the galactic wind, and perform a Faraday rotation measure analysis in order to find the magnetic field structure around the galaxies.

For our study, we chose two nearby starburst dwarf galaxy NGC 1569 and NGC 4449, both of which are well-studied and bright in the radio-continuum. In Chap. 2, we give a brief observational overview of these two objects, wherein we mention the important results from earlier studies done throughout the observable spectrum. Chap. 3 describes the most important astrophysical theories used for our analysis, for e.g. - synchrotron emission and cosmic ray electron dynamics. In Chap. 4, we describe the observational set-up and parameters, and the entire data-reduction process. In Chap. 5, we present our results and analysis and finally discuss these in Chap. 6, ending with our conclusions and some reflections on the bright future prospects of this exciting puzzle of the Universe.

[1] http://www.lofar.org/
[2] http://www.skatelescope.org/

Chapter 2

Observational Overview

2.1 NGC 1569

NGC 1569 is a starburst dwarf irregular galaxy, located in the Camelopardalis constellation. It is well-studied, having been observed for decades in different wavelength regimes – from X-rays to radio. Table 2.1 shows the properties of the galaxy. Figure 2.1 gives a multi-wavelength view of the object.

Martin et al. (2002) presented results from high-spatial-resolution observations of NGC 1569 with the *Chandra*. Figure 2.1, top left panel, shows a composite three-colour image, where the *Chandra* X-ray emission is in *green*, Hα emission from the KPNO 2.1 m telescope in *red* and optical 6450 Å continuum from the KPNO 2.1 m telescope in blue. Contours show the 21 cm neutral hydrogen column density at levels of $1 \times 10^{21}\,\mathrm{cm}^{-2}$(*heavy line*), $4 \times 10^{21}\,\mathrm{cm}^{-2}$(*solid line*) and $7 \times 10^{21}\,\mathrm{cm}^{-2}$(*dashed line*). They confirmed the strong spatial correlation between the extended X-ray emission and the Hα filaments, which was previously noted by Heckman et al. (1995) and della Ceca et al. (1996). They discovered that the halo consists of two X-ray components. The brighter 0.3 keV component, that comes from the highest X-ray surface brightness regions of the halo, is associated with the halo shock generated by the outflow. X-ray emission was detected over the full extent of the Hα nebula but not convincingly beyond it. They proposed that the X-ray emission might come from the mixing layers between the shock and the bubble interior rather than the actual shock front. In either scenario, the presence of the shock implies that the wind encounters a gaseous halo that was previously unrecognised. The wind-halo interaction significantly boosts the X-ray luminosity of the

Parameter	NGC 1569	NGC 4449
Coordinates (J2000.0)	RA:04h 30m 49.0s Dec: +64d 50m 53s	RA:12h 28m 11.1s Dec: +44d 05m 37s
Object Type	G	G
Classifications	Dwarf irregular, Starburst	Dwarf irregular. Starburst
Redshift	-0.000347	0.000690
Galactic Latitude (deg)	11.2417452	72.400729
Distance (Mpc)	3.36	3.69
D_{25} (arcmin)	3.6×1.8	6.2×4.4
Magnitude (B band)	-17	-18.2

Tab. 2.1: Properties of NGC 1569 and NGC 4449 (NASA Extragalactic Database).

galaxy. They argued that the wind in NGC 1569 is likely to be powerful enough to blow through this halo and escape the galactic potential. Additionally, they presented a diagram (Figure 2.2) showing the relevant geometry of the disk and wind. Gas kinematics indicate that north (south) of the major axis the wind is pointed away from (toward) our line of sight (Israel & van Driel, 1990; Heckman et al., 1995; Martin, 1999).

Gil de Paz et al. (2007) presented images, integrated photometry, surface-brightness and colour profiles for a total of 1034 nearby galaxies observed by the *Galaxy Evolution Explorer (GALEX)* satellite in its far-ultraviolet (FUV; $\lambda_{eff} = 1516\,\mathring{A}$) and near-ultraviolet (NUV: $\lambda_{eff} = 1516\,\mathring{A}$) bands. NGC 1569 was a part of the sample. Figure 2.1, top right panel, shows a false-colour RGB map of the galaxy. Shown in green is the RC3 D25 ellipse, which was originally derived from B-band photometry. Asymptotic magnitudes and colours along with concentration indices had been obtained. A morphological classification of the profiles was also carried out. According to the shape of the UV surface brightness profile, NGC 1569 was morphologically classified as V-type, i.e., it has a de Vaucouleurs profile where the brightness is proportional to $R^{1/4}$, R being the distance from the centre (de Vaucouleurs, 1977).

In the optical regime, the multi-burst structure of NGC 1569 was first shown by Vallenari & Bomans (1996) and later optical studies confirmed this and investigated the complex star formation history of this object in detail. Grocholski et al. (2008) presented deep *Hubble Space Telescope (HST)* ACS/WFC photometry of NGC 1569. Figure 2.1, middle left panel, shows the final image. These data allow them, for the first time, to unequivocally detect the tip of the red giant branch (RGB) and hence revise the distance to the galaxy. The distance was found to be 3.36±0.20 Mpc, significantly greater than the previously assumed distance of 2.2 ± 0.6 Mpc (Israel, 1988). NGC 1569 was previously thought to be an isolated galaxy, due to its shorter distance, but this new distance firmly established it as a member of the IC 342 group of galaxies. The higher density environment might help explain the starburst nature of NGC 1569, since starbursts are often triggered by tidal interactions with other galaxies. Also, the increased distance altered the then existing estimates for its star formation rate (SFR) and super star cluster (SSC) masses that were based on the old distance. The new masses of the three massive SSCs in the galaxy NGC 1569−A1, NGC 1569−A2 and NGC 1569−B are $6.0 \times 10^5 M_\odot$, $6.7 \times 10^5 M_\odot$ and $6.7 \times 10^5 M_\odot$, respectively, 53% greater than those previously calculated by Larsen et al. (2008). In contrast to previous work on SFRs of NGC 1569 (refer to next paragraph), their data, which were significantly deeper and covered a much larger area, show a well-populated, fully formed RGB, suggesting that star formation in NGC 1569 began ≥ 2 Gyr ago. In their next paper, Grocholski et al. (2012) described this star formation history (SFH) in further detail. They now presented the evolution of the galaxy over a full Hubble time, focusing their analysis on the outer region of the galaxy, which is largely devoid of young stars. They found out that NGC 1569 cannot be treated as a simple stellar population (single age and single metallicity), as it has a more complex SFH. They then derived the full SFH by using a newly developed code called SFHMATRIX. They found the best-fitting distance to be 3.06 ± 0.18 Mpc. According to their model, star formation in the outer region of the galaxy began ≈ 13 Gyr ago and lasted until ≈ 0.5 Gyr ago. The initial burst was followed by a relatively low, constant SFR until $\approx 0.5 - 0.7$ Gyr ago, when there might have been a short, low intensity burst of star formation. The distance and line-of-sight velocity of NGC 1569 suggested that it

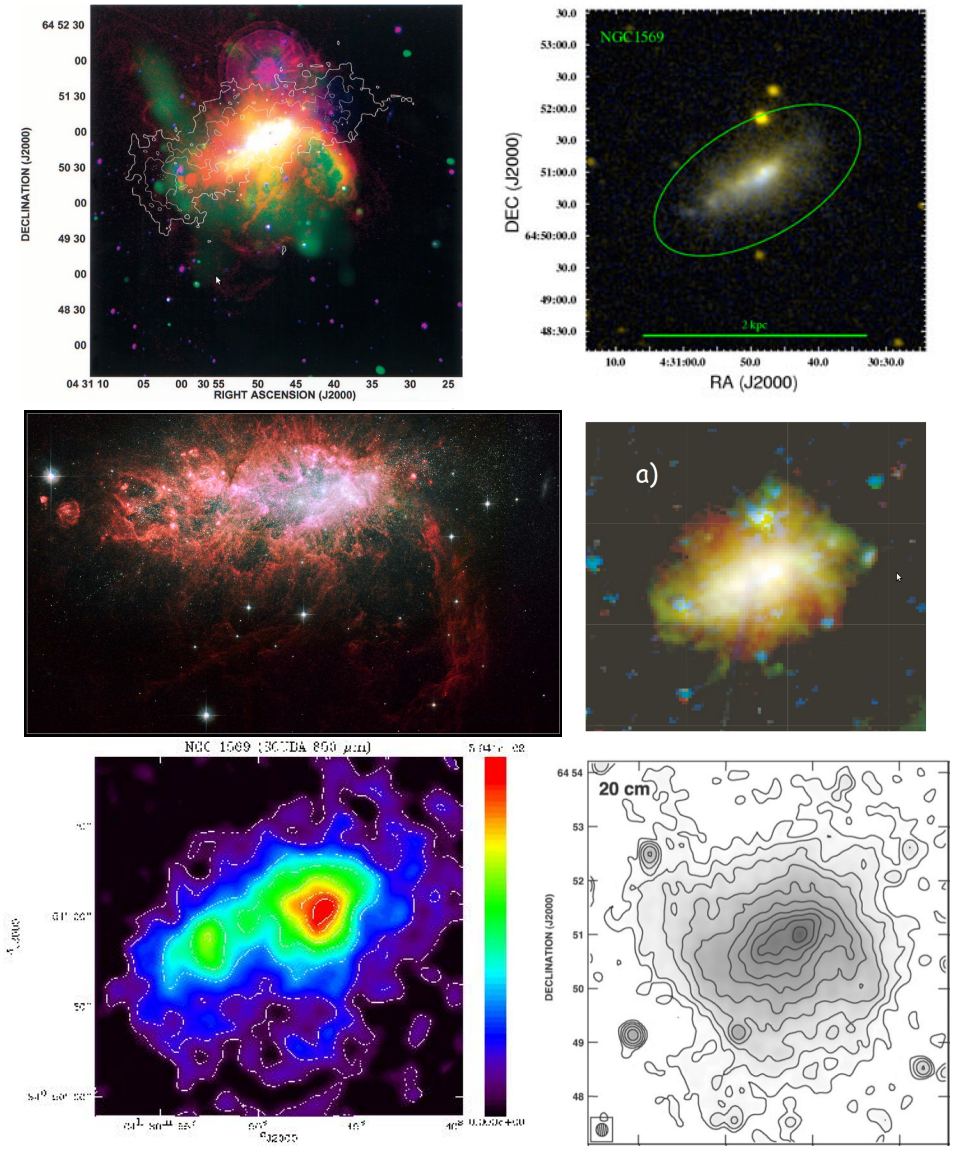

Fig. 2.1: Multi-frequency view of NGC 1569: [Top left] *Chandra* composite three-colour image, X-ray emission in *green*, Hα emission in *red* and 21 cm neutral hydrogen contours (Martin et al., 2002); [Top right] False-colour *GALEX* images at FUV-NUV (Gil de Paz et al., 2007); [Middle left] HST optical image (Grocholski et al., 2008, 2012); [Middle right] AKARI artificial 3-colour mid-infrared image (Onaka et al., 2010); [Bottom left] SCUBA map in the submm regime (Galliano et al., 2003; Lisenfeld et al., 2002); [Bottom right] WSRT total intensity radio image at 20 cm (Kepley et al., 2010).

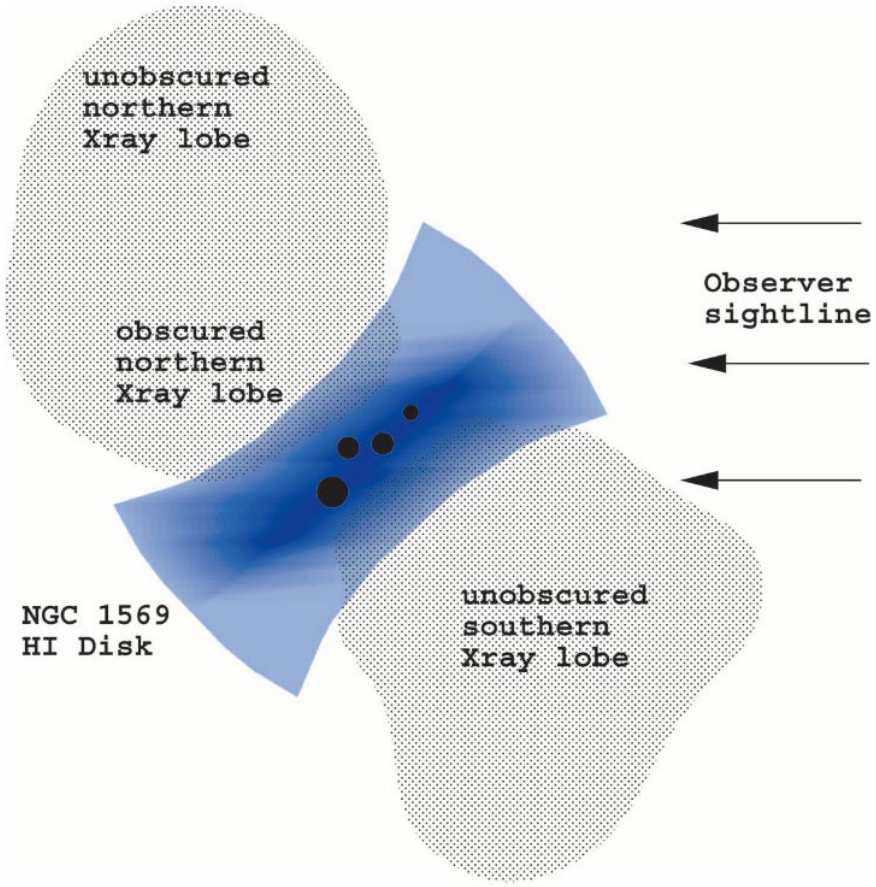

Fig. 2.2: NGC 1569: Geometry of the disk and outflow (Martin et al., 2002)

moved through the IC 342 group atleast in the past few Gyr. This could be the reason for the extended low-level star formation seen in its outer region. They compared their work with recent work by McQuinn et al. (2010) and Ryś et al. (2011) and found no evidence for radial population gradients in the old population of the galaxy. Hence, they suggested that their results for the outer region are representative of the old stellar population throughout the galaxy.

Angeretti et al. (2005) presented interesting results on the complex star formation history (SFH) of NGC 1569. The data were obtained with the *HST* NICMOS/NIC2, in the F110W(J) and F160W(H) near-infrared (NIR) filters and interpreted with the synthetic colour-magnitude diagram method. The best fit to the data was found by assuming three episodes of activity in the last 1-2 Gyr. The most recent and strong episode constrained by these NIR data started $\approx 3.7 \times 10^7$ yr ago ended $\approx 1.3 \times 10^7$ yr ago, although they could not exclude the possibility that up to three SF episodes occurred in this time interval. The average SFR density of the episode is $\approx 3.2\, M_\odot\, \mathrm{yr}^{-1}\, \mathrm{kpc}^{-2}$, in agreement with literature. A previous episode produced stars between $\approx 1.5 \times 10^8$ and $\approx 4 \times 10^7$ yr ago, with a mean SFR about two-thirds lower than the mean SFR of the youngest episode. An older SF episode occurred about 1 Gyr ago. All these SFRs were found by them to be 2-3 orders of magnitude higher than those derived for late-type dwarfs of the Local Group. Pasquali et al. (2011) also confirmed the multiple bursts

scenario, but found that the most recent instantaneous burst occurred about 4 Myr ago. The star-formation rate was found to be $0.4\,M_{\odot}\mathrm{yr}^{-1}$.

Onaka et al. (2010) investigated the processing and destruction of the unidentified infrared (UIR) band carriers in an outflow from NGC 1569, based on observations of the galaxy in 6 infrared bands (3.2, 4.1, 7, 11, 15, and 24 μm) with the infrared camera (IRC) onboard the *AKARI* satellite. Near to mid-infrared (2-13 μm) spectroscopy of an Hα filament was also carried out with the IRC. Figure 2.1, middle right panel, shows the AKARI artificial 3-colour mid-infrared image. The study of UIR bands in low-metallicity dwarf galaxies is important because in such environments, the UIR band carriers, like carbon-rich AGB stars, may not be fully developed (Galliano et al., 2008). The metallicity of NGC 1569 is slightly above the threshold for the presence of UIR bands, and previous studies (Madden et al., 2006; Tokura et al., 2006) had already detected UIR bands. These new observations could shed light on the the distribution and possible spatial variations in the UIR bands. They found that the extended structure associated with an Hα filament appeared bright at $7\,\mu$m UIR band. Follow-up spectroscopic observations with the IRC confirmed the presence of 6.2, 7.7, and $11.3\,\mu$m emission in the filament. The filament spectrum exhibited stronger $11.3\,\mu$m emission compared to the $7.7\,\mu$m band. The near-infrared spectrum ($2.5-5\,\mu$m) of the filament also indicated the presence of excess continuum emission. The Hα filament might have been formed by the galactic outflow originating from the star-formation activity in the disk of NGC 1569. They estimated the destruction timescale of the UIR band carriers in the outflow to be $\approx 1.3\times10^{3}\,$yr, much shorter than the timescale of the outflow, which is $\approx 5.3\,$Myr. Therefore it is unlikely that the band carriers survive the outflow environment. Alternatively, they suggested that the band carriers in the filaments may be produced by the fragmentation of large carbonaceous grains in shocks, which produce the Hα emission. The NIR excess continuum emission cannot be accounted for by free-free emission alone and a hot dust contribution may be needed.

The absorption of stellar radiation by dust and its subsequent re-emission in the infrared (IR) to the submillimeter (submm) regime is a fundamental process controlling the heating and cooling of the interstellar medium (ISM). Galliano et al. (2003) presented new 450 and $850\,\mu$m SCUBA data of NGC 1569. They constructed the mid-infrared to millimeter spectral energy distribution (SED) of the galaxy, using ISOCAM, ISOPHOT, IRAS, KAO, SCUBA and MAMBO data, and model the SED in order to explore the nature of the dust in low metallicity environments. Figure 2.1, bottom left panel, shows the SCUBA map at $850\,\mu$m, tracing the cold dust continuum. Its morphology is similar to the Hα emission. Their results show that the dust properties are different in this low metallicity galaxy compared to other more metal-rich galaxies. The dust emission is dominated by small grains (of radius $\approx 3\,$nm). The redistribution of large dust grains into smaller sizes is supported by the shock model of Jones et al. (1996) and is consistent with an ISM heavily influenced by supernova activity. Also, they found that the SED exhibit a submm excess in emission (after subtraction of the contamination from molecular lines and radio continuum). This component which accounts for 40 to 70% of the total dust mass in the galaxy ($1.6-3.4\times10^{5}M_{\odot}$) could be produced by the presence of ubiquitous very cold dust ($T=5-7\,$K) that could hide in dense clumps in this galaxy (size $\simeq$ a few pc). This total dust mass value that they deduced is higher than what was previously found by investigators who did not take into account the submm part of the

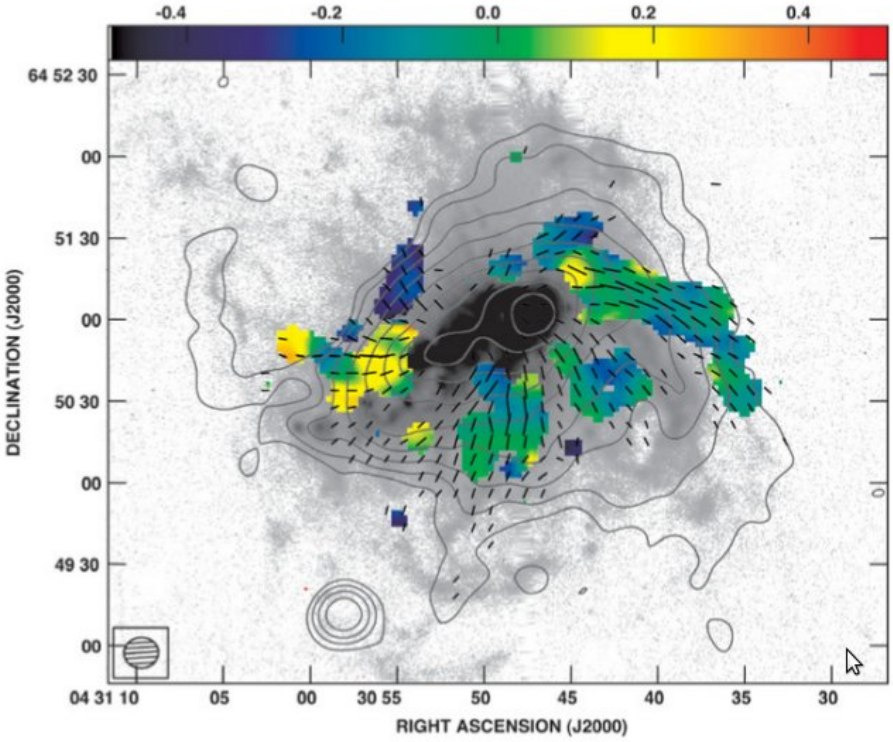

Fig. 2.3: Rotation measures between the 14″ resolution 6 cm and 3 cm data (colour), magnetic field vectors derived from the 3 cm data, and the contours of 3 cm data overlaid on an Hα image. The colour bar is in units of 10^3 rad m^{-2} (Kepley et al., 2010).

SED constrained by SCUBA observations. Furthermore, they generated an extinction curve for NGC 1569 and found that it resembles observed extinction curve of some regions in the Large Magellanic Cloud (LMC).

Finally, we come to the radio regime, where the latest work on NGC 1569 was presented by Kepley et al. (2010). They made the first radio continuum polarisation observations of this galaxy at 20 cm, 13 cm, 6 cm and 3 cm. Figure 2.1, bottom right panel, shows their WSRT total power image at 20 cm, which confirms the presence of an extended radio continuum halo. These observations showed for the first time that the radio continuum features are associated with the Western Hα arm at wavelengths shorter than 20 cm. They confirmed that the spectral index trends in this galaxy supports the theory of a convective wind at work. Strong polarised emission at 3 cm and 6 cm and weak polarised emission at 13 cm and 20 cm were detected. They derived a total equipartition magnetic field strength of 38 μG in the core of the galaxy and $10 - 15\,\mu$G in the halo. The magnetic field was found to be mostly random in the core, whereas the ordered field ($\approx 3 - 9\,\mu$G) was the strongest in the halo. The ordered magnetic field was found to be closely associated with the Hα bubbles and filaments. They suggested that a supernova-driven dynamo may be operating in this galaxy. Furthermore, they performed a rotation measure analysis in order to find the magnetic field structure in the galaxy (shown in Figure 2.3). They deduced that the magnetic field structure appeared to be dominated

by field loops being drawn out of the disk of the galaxy by an outflow of hot gas, but the magnetic field in turn might be aiding the outflow channelling gas out of the galaxy disk. From their work, it is all but evident that lower frequency observations were needed to determine if dwarf galaxies like NGC 1569 could have played a significant role in magnetizing the intergalactic medium (IGM).

2.2 NGC 4449

NGC 4449 is an irregular dwarf galaxy with many regions of star formation. It was discovered back in 1788 by Sir William Herschel. It is located in the Canes Venatici constellation. Table 2.1 shows the properties of the galaxy. Like NGC 1569, NGC 4449 has also been studied over essentially the whole electro-magnetic spectrum. It reveals interesting and rather unusual characteristics. Figure 2.4 gives a multi-wavelength view of the object. The observed morphology and absolute size are remarkably similar to our neighbour galaxy LMC. Also, the morphology and kinematics of the H I gas suggests a tidal interaction with the nearby dwarf galaxy DDO 125 (Theis & Kohle, 2001), and may explain the high-star formation rate and the huge H I streamers surrounding the galaxy (Bajaja et al., 1994; Hunter et al., 1998).

Summers et al. (2003) presented analysis of X-ray data of NGC 4449, observed with the *Chandra* satellite. They found 24 distinct point sources, within the D_{25} ellipse of the galaxy which were either supernova remnants, X-ray binaries or supersoft sources. The morphology of the diffuse X-ray emission was found to be similar to the observed Hα emission. The X-ray emission appeared to fill cavities in the Hα emission, which, they suggest, is indicative of an expanding super-bubble. They found the galaxy to have a huge H I halo extending out to $\sim 40\,\mathrm{kpc}$, which might prevent the ejection of the metal-enriched material in the bubble, into the IGM. They calculated the current expansion speed of the bubble to be $\sim 220\,\mathrm{km\,s^{-1}}$, which is less than the estimated escape velocity from the H I halo. However, the present temperatures of the gas components imply that they can escape the gravitational potential of the galaxy, and hence, can eject metal-enriched, hot gas into the IGM. The crucial factors are the time for which energy injection can be maintained and the actual distribution of H I in the halo of the galaxy.

Annibali et al. (2008) presented photometry with the Advanced Camera for Surveys (ACS) on the Hubble Space Telescope of stars NGC 4449. The features observed in the colour-magnitude diagrams (CMDs) implied a variety of stellar ages up to at least 1 Gyr, and possibly as old as a Hubble time. Also, massive, young and intermediate-age stars tend to be concentrated toward the galactic center, while old stars are present everywhere. Furthermore, they detected an interesting resolved star cluster on the west side of the galaxy, surrounded by a symmetric tidal or spiral feature consisting of young stars. The positions of the stars in NGC 4449 younger than 10 Myr are strongly correlated with the Hα emission.

More recently, Karczewski et al. (2013) presented an integrated photometric spectral energy distribution (SED) of NGC 4449, from the far-ultraviolet (FUV) to the sub-millimetre (submm) bands, including new observations made by the *Herschel* Space Observatory, as part of the Dwarf Galaxy Survey (Madden et al., 2013). They also included integrated UV photometry from the Swift Ultraviolet and Optical Telescope,

using a measurement technique which is appropriate for extended sources with coincidence loss. The available multi-wavelength data were analysed to infer a range of ages, metallicities and star formation rates for the underlying stellar populations, and also the composition and the total mass of dust in the galaxy. For their analysis, they used results from previous studies, the available multi-wavelength data, the spectral fitting code STARLIGHT and a simple chemical evolution code to construct a photoionisation and radiative transfer model of NGC 4449 through an iterative scheme. Their results showed that the majority of the stellar mass of the galaxy resides in old ($\geq$ 1 Gyr) and metal-poor ($Z/Z_{\odot} \sim 0.2$) populations. The first onset of star formation activity took place approximately 12 Gyr ago. They modelled the entire stellar component self-consistently along with a mixture of carbon and silicate dust. This simple chemical evolution model, suitable for a star-forming galaxy, yielded a total dust mass of $2.9 \pm 0.5 \times 10^6\,M_{\odot}$ and gave results that are consistent with the carbon to silicate dust mass ratio of 1:3 inferred for the LMC (Weingartner & Draine, 2001). Additionally, they inferred a recent star formation rate of $0.4\,M_{\odot}\mathrm{yr}^{-1}$ and a total stellar mass of $\approx 1 \times 10^6\,M_{\odot}$ emitting with a bolometric luminosity of $5.7 \times 10^9\,L_{\odot}$. They also deduced a dust to gas mass ratio of 1/190, within the modelled region of 3.3 kpc radius. Their model did not account for cold dust (refer to next paragraph), which could have a significant effect on this ratio.

To study the relation between cold dust and molecular gas in low metallicity environments, Böttner et al. (2003) had presented observations of NGC 4449 at 850 μm and 450 μm obtained with the Submillimetre Common-User Bolometer Array (SCUBA) at the James Clarke Maxwell Telescope (JCMT). They were able to fit the observed SED well with Plankians of three dust components with temperatures of 16, 39 and 168 K. Most of the dust was required to be at 16 K, and hence the dust mass was found to be dominated by the cold dust component. They derived a total dust mass of $\sim 3.8 \times 10^6\,M_{\odot}$. Comparison with Carbon monoxide (CO) observations and Hα emission showed a good coincidence of the cold dust and the molecular gas. CO is commonly used as a tracer for molecular gas because molecular hydrogen lacks strong emission lines which could determine the column density.

Coming to the radio regime, the latest study of NGC 4449 was presented by Chyży et al. (2000). They presented high-resolution observations of the total power and polarized radio continuum emission at 8.46 and 4.86 GHz using the Karl G. Jansky Very Large Array (VLA). Since this galaxy rotates slowly and has chaotic motion, dynamo-induced large-scale magnetic fields were not expected. Surprisingly however, they found strong, galaxy-scale regular magnetic fields. The equipartition strength of the ordered field reached 8 μG and that of the total magnetic field 14 μG, which is comparable to that in radio-bright spirals. As can be seen in Figure 2.4 (third row, right panel), the magnetic vectors form radial "fans" in the core, fragments of a spiral pattern towards the edges of the galaxy. They showed that these structures are associated with large regions of systematic Faraday rotation, implying genuine galaxy-scale regular magnetic fields rather than random anisotropic ones compressed and stretched by gas outflows. A non-standard dynamo theory is required to explain the observed magnetic field strength and structure, although it is unknown what kind of magnetic field geometry can be produced in slowly and chaotically rotating objects. They concluded that the so-far-neglected role of magnetic fields for the dynamics and star formation in dwarf irregulars needed to be revised.

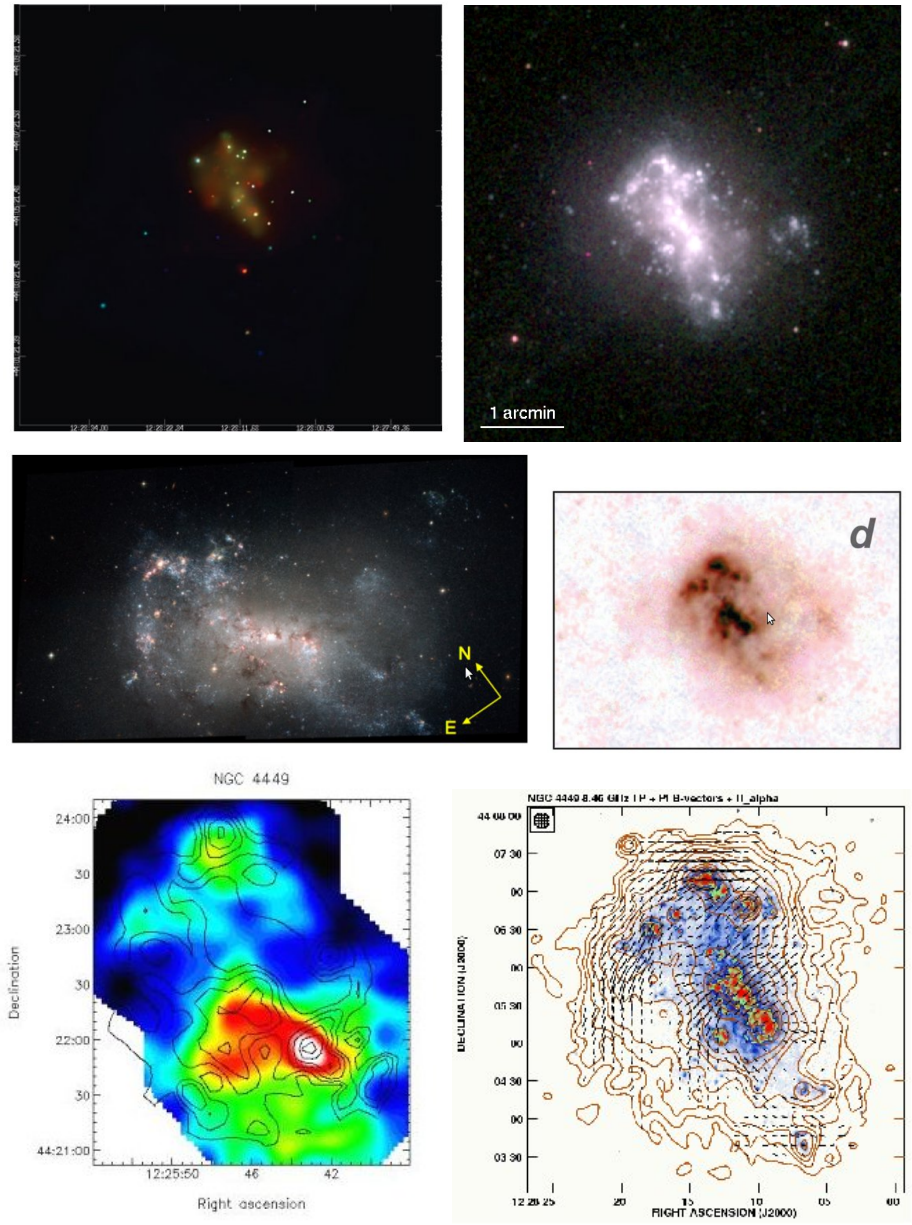

Fig. 2.4: Multi-frequency view of NGC 4449: [Top left] Adaptively smoothed three-colour *Chandra* X-ray image (red, 0.3-0.8 keV; green, 0.8-2.0 keV; blue, 2.0-8.0 keV) (Summers et al., 2003); [Top right] *Swift*/UVOT image in Ultraviolet (Roming et al., 2005); [Middle left] HST optical image (Annibali et al., 2008); [Middle right] *Herschel*/PACS false-colour (R,G,B) broad-band image in FIR (Karczewski et al., 2013); [Bottom left] SCUBA map in the submm regime, 850 μm map with CO(1-0) contours superimposed (Böttner et al., 2003); [Bottom right] The total power contour map at radio (8.46 GHz) with observed B-vectors of polarized intensity (taken as perpendicular to E-vectors) (Chyży et al., 2000), superimposed onto the coloured Hα image of Bomans et al. (1997).

2.3 NGC 1569 & NGC 4449: comparison and relevance

From all the various studies discussed above, it is important to now briefly compare the main physical properties of the two galaxies. Both the galaxies are dwarf irregulars, resembling the Magellanic Clouds but lacking any clear spiral structure. Both are at comparable distances of a few megaparsecs, and the B-band absolute magnitudes are also comparable, NGC 4449 being slightly more luminous than NGC 1569. With a total mass of the order of $10^9\,M_\odot$, NGC 4449 is also more massive than NGC 1569 ($\sim 10^8\,M_\odot$). In both the galaxies, the first onset of star-formation activity took place more than 12 Gyr ago. However. NGC 1569 seems to have had a more complex star-formation history than NGC 4449. The former has had multiple star-forming episodes over the past 1 Gyr, of which the most recent one occurred about 4 Myr ago. The average SFR of this episode was $0.4\,M_\odot \mathrm{yr}^{-1}$. Detection of very high-mass stars ($\sim 40\,M_\odot$) in NGC 4449 implies that star formation was active 5 Myr ago, and possibly is still ongoing. The absence of significant gaps in the CMDs suggests also that star-formation has been mostly continuous over the last 1 Gyr. However, the SFR of NGC 4449 is the same as that of NGC 1569.

In the previous two sections, we have reviewed the properties of our target sources in all wavelengths for the purpose of analysis, interpretation and understanding of the radio data in this work. Multi-wavelength studies of the sources are crucial to paint a complete physical picture of the systems. X-ray observations give information about the hot gas in the interstellar medium of a galaxy. In a dwarf galaxy, the hot gas can expand as a bubble and break out of the gaseous disk into the halo. The radio synchrotron emission comes from cosmic-ray electrons that are ejected by exploding supernovae and gives us information about magnetic fields. Interaction of the hot gas with the magnetic fields affect the properties in the halo of the galaxy. There is no way to determine the distance of a radio source from radio observations alone, yet distance is required to convert the apparent properties of a source (e.g flux density and angular extent) into intrinsic properties of the source (luminosity and linear dimensions). Therefore. optical measurements are required. The star-formation histories, obtained from analysis of the spectral energy distribution from the UV to the submm bands, is essential to interpret the spectral characteristics found from radio observations. The absorption of stellar radiation by dust and its subsequent re-emission in the IR to the submm regime is a fundamental process controlling the heating and cooling of the interstellar medium ISM. Therefore, dust emission affects the total thermal emission from the galaxy, which is important in order to separate the non-thermal emission from the total emission at radio wavelengths. This physical understanding gathered from multi-wavelength studies will help in analysing and interpreting the results presented later in Chap. 5.

Chapter 3

Theoretical Background

3.1 Synchrotron radiation

Synchrotron radiation is the emission when relativistic electrons gyrate in a magnetic field. It is one of the mechanisms responsible for the *non-thermal* radio emission of our Galaxy, supernova remnants and extragalactic radio sources.

3.1.1 Total emitted power from a single electron

When a relativistic electron, with velocity factor $\beta = v/c$ and Lorentz factor γ, moves in a magnetic field B, Maxwell's equations of electrodynamics show that the resulting motion is *helical*. The frequency of the rotation, gyrofrequency, is

$$\omega_B = \frac{qB}{\gamma mc}, \tag{3.1}$$

where m is electron mass and c is speed of light. For an isotropic distribution of electron velocities, the total emitted power, P, is given by:

$$P = \frac{4}{3}\sigma_T c\beta^2\gamma^2 U_B, \tag{3.2}$$

where $\sigma_T = 8\pi {r_0}^2/3$ is the Thomson cross-section, and U_B is the magnetic energy density $U_B = B^2/8\pi$.

The total power, perpendicular and parallel to the magnetic field, emitted per unit frequency ω, by a single relativistic electron ($\beta \approx 1$), is given by:

$$P_{\perp,\parallel}(\omega) = \frac{\sqrt{3}q^3 B\sin\alpha}{4\pi mc^2}[F(x) \pm G(x)], \tag{3.3}$$

where α is the pitch angle, $F(x)$ and $G(x)$ are the "kernel" functions defined by:

$$F(x) \equiv x\int_x^\infty K_{\frac{5}{3}}(\xi)d\xi, \qquad\qquad G(x) \equiv xK_{\frac{2}{3}}(x), \tag{3.4}$$

and $F(x)$ is shown in Figure 3.1. K is a modified Bessel function and $x \equiv \omega/\omega_c$ (see Eq. 3.5). The total power $P(\omega)$ is given by the sum of $P_\parallel(\omega)$ and $P_\perp(\omega)$. As seen in the

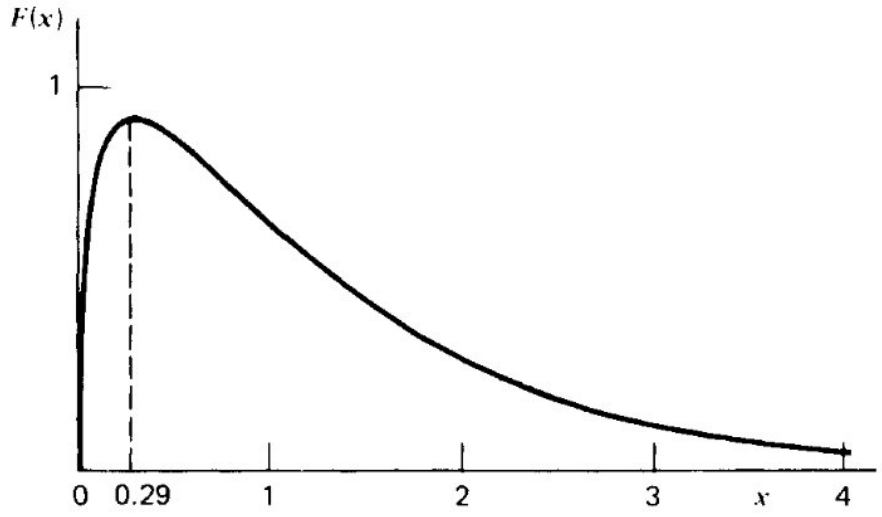

Fig. 3.1: Function describing the total power spectrum of synchrotron emission by a single relativistic electron. Here $x \equiv \omega/\omega_c$. Taken from Rybicki & Lightman (1986)

figure, the spectrum of synchrotron radiation sharply peaks at the critical frequency, ω_c, defined by:

$$\omega_c \equiv \frac{3}{2}\gamma^3 \omega_B \sin\alpha, \tag{3.5}$$

where ω_B refers to the gyrofrequency in Eq. 3.1. In a simple approximation, it can be assumed that an electron radiates away its energy at this critical frequency. The spectral index s is related to the particle distribution index p by $s = \frac{p-1}{2}$ (see Sec. 3.1.2). For detailed derivations, refer to Rybicki & Lightman (1986) or Longair (2011).

3.1.2 Power-law electron spectrum

The energy spectra of cosmic ray electrons can be often approximated by power-law distributions, and subsequently the spectra of non-thermal sources can often be well-represented by power-law spectra. For a distribution of relativistic electrons with a particle distribution index p, the number density of electrons with energies between E and $E + dE$ can be expressed by:

$$N(E)dE = \kappa E^{-p} dE. \tag{3.6}$$

To obtain the power per unit volume per unit frequency, $P_{tot}(\omega)$, for such a power-law distribution of electrons, F(x) and G(x) functions in Eq. 3.4 need to be integrated over x first. It can be then shown that:

$$P_{tot}(\omega) = \frac{\sqrt{3} q^3 \kappa B \sin\alpha}{2\pi m c^2 (p+1)} \Gamma\left(\frac{p}{4} + \frac{19}{12}\right) \Gamma\left(\frac{p}{4} - \frac{1}{12}\right) \left(\frac{mc\omega}{3qB\sin\alpha}\right)^{-(p-1)/2} \tag{3.7}$$

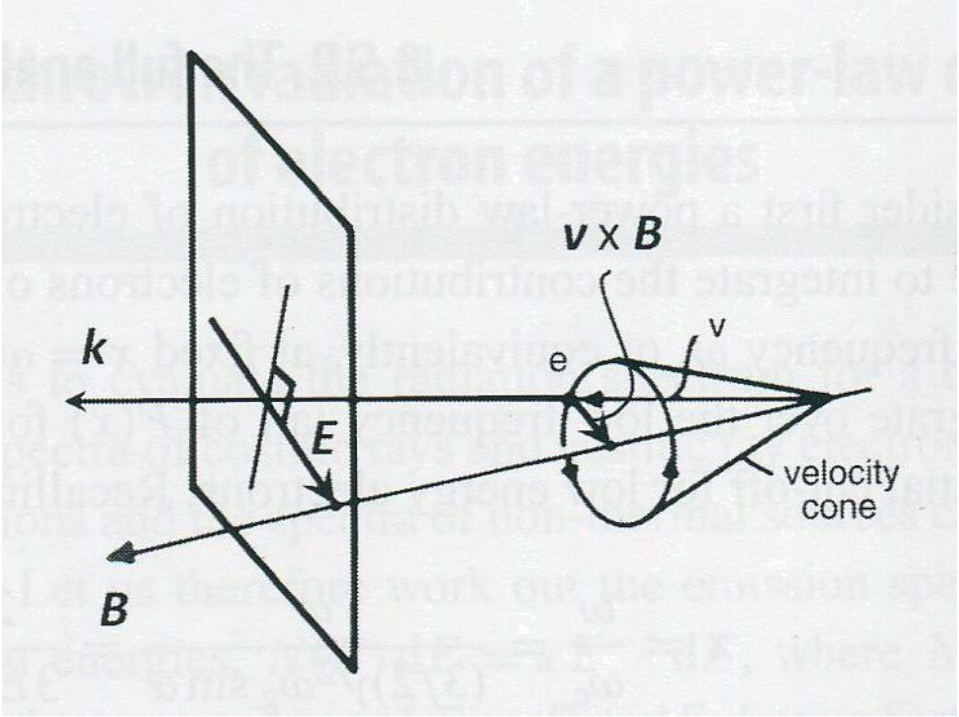

Fig. 3.2: The geometry of the velocity cone of an ultra-relativistic electron and the polarisation of the received radiation. Taken from Longair (2011).

3.1.3 Polarisation properties

The radiation from a single non-relativistic electron is circularly polarised when viewed along the magnetic field lines, but in general, when viewed at any angle, the radiation is elliptically polarised. In the case of relativistic electrons, significant radiation is observed only if the electron trajectory lies within an angle $1/\gamma$ of the line of sight. To understand the polarisation properties of synchrotron radiation, the concept of the *velocity cone* is very helpful. It is the cone described by the velocity vector $\mathbf{v}$ of the electron as it spirals around the magnetic field at the relativistic gyrofrequency (Eq. 3.1). Figure 3.2 illustrates the case of those electrons with velocity cones lying precisely along the line of sight of the observer. The radiation from a single electron is elliptically polarised because the component parallel to $\mathbf{B}$ has a different time-dependence within each pulse as compared with that of the perpendicular component. However, when there is a distribution of pitch angles, the elliptical component will cancel out, as velocity cones will contribute equally from both sides of the line of sight. Hence, the radiation will be partially linearly polarised, and we obtain the correct expression of the radiation by its powers per unit frequency $P_{\parallel}(\omega)$ and $P_{\perp}(\omega)$, and neglect their time variation through the pulse. The fractional polarisation is defined to be

$$\Pi(\omega) = \frac{P_{\perp}(\omega) - P_{\parallel}(\omega)}{P_{\perp}(\omega) + P_{\parallel}(\omega)}. \tag{3.8}$$

Inserting the expressions for the powers given in Eq. 3.3. we find

$$\Pi(\omega) = \frac{G(x)}{F(x)}. \tag{3.9}$$

For particles with a power-law distribution of energies, described by Eq. 3.6, the fractional polarisation can be shown to be

$$\Pi(\omega) = \frac{p+1}{p+\frac{7}{3}}. \tag{3.10}$$

Thus, for a typical of the exponent of the energy spectrum of the electrons, p = 2.5, the fractional polarisation of synchrotron radiation is expected to be about 72%, which is rather high. The assumption here was that **B** is a uniform magnetic field and that there are no depolarizing effects (refer to 3.3.2) such as beam or Faraday depolarization.

3.2 Cosmic Ray Electron Dynamics

3.2.1 Energy loss processes for high-energy electrons

Cosmic ray electrons are subject to *five* kinds of energy loss processes – *Ionisation losses, Bremsstrahlung, Adiabatic losses, Synchrotron radiation* and *Inverse Compton Scattering*. These mechanisms cause distortions of their injection energy spectra as they *diffuse* from their sources through the ISM, and also provide information about their life histories. The loss processes essentially involve interactions with matter, magnetic fields and radiation.

Ionisation Losses

When cosmic ray electrons move through a neutral medium, they can scatter with the electrons of the atoms in the medium, thus ionising the medium and in the process losing energy. The ionisation loss rate for the case of atomic hydrogen is (Blumenthal & Gould, 1970; Longair, 2011):

$$-\left(\frac{\mathrm{d}E}{\mathrm{d}t}\right)_i = 7.64 \times 10^{-15} n(3\ln\gamma + 19.8)\ \mathrm{eVs}^{-1}, \tag{3.11}$$

where n is the number density of hydrogen atoms. Ionization losses are especially important astrophysically in the heating and ionisation of cold, dense molecular clouds in the ISM.

Bremsstrahlung

Electrons travelling at relativistic velocities through an ionised plasma lose energy due to the Coulomb (electrostatic) interaction with the charged particles of the plasma. The loss rate of an electron in a fully ionised hydrogen plasma is given by (Heitler, 1954;

Longair, 2011):

$$-\left(\frac{\mathrm{d}E}{\mathrm{d}t}\right)_{brems} = 7.0 \times 10^{-23} nE(\ln\gamma + 0.36)\ \mathrm{eVs}^{-1}, \tag{3.12}$$

where n is the number density of the hydrogen plasma. Relativistic Bremsstrahlung makes a significant contribution to the low energy γ-ray emission of the ISM (Strong et al., 2000).

Adiabatic losses

Adiabatic losses come into play, if the electrons are confined within an expanding volume and if the time-scale of the expansion is of the same order as the time the electrons have been confined in the volume. In the case of a uniformly expanding sphere of radius R, the loss rate for cosmic ray electrons within the sphere is given by (Kardashev, 1962; Longair, 2011):

$$-\left(\frac{\mathrm{d}E}{\mathrm{d}t}\right)_{ad} = \left(\frac{1}{R}\frac{\mathrm{d}R}{\mathrm{d}t}\right) E. \tag{3.13}$$

If the particles have always been confined within a source during its expansion, adiabatic losses are always important.

Synchrotron radiation

Synchrotron radiation is a dominant loss process in the regime of number densities and magnetic fields ($n \approx 10^{-3}\,\mathrm{cm}^{-3}, B \approx 1\,\mu\mathrm{G}$) of our interest. As described in Sec. 3.1, the loss rate is given by Eq. 3.2:

$$-\left(\frac{\mathrm{d}E}{\mathrm{d}t}\right)_{synch} = \frac{4}{3}\sigma_T c\beta^2\gamma^2 U_B = 6.6 \times 10^4 \gamma^2 B^2\ \mathrm{eVs}^{-1}. \tag{3.14}$$

Inverse Compton scattering

In inverse Compton scattering, ultra-relativistic electrons scatter photons, which gain energy in the process at the expense of the kinetic energy of the electrons. The loss rate of a cosmic ray electron in a radiation field of energy density U_{rad} is given by (Longair, 2011):

$$-\left(\frac{\mathrm{d}E}{\mathrm{d}t}\right)_{IC} = \frac{4}{3}\sigma_T c\gamma^2 U_{rad}, \tag{3.15}$$

where $\sigma_T = 8\pi {r_0}^2/3$ is the Thomson cross-section. There is a remarkable similarity between synchrotron (Eq. 3.14) and inverse Compton (Eq. 3.15) loss rates. The reason for this is that the energy loss rate depends upon the electric field which accelerates the electron in its rest frame, irrespective of the origin of that field. In the case of synchrotron radiation, the electric field is the $(\mathbf{v} \times \mathbf{B})$ field due to the motion of the

electron through the magnetic field, while in the case of inverse Compton scattering, it is the sum of the electric fields of the electromagnetic waves incident upon the electron.

Inverse Compton scattering is important whenever high-energy electrons propagate through a radiation field. In our case, inverse Compton losses are important because the radiation field is strong due to the starbursts in the galaxies. Part of the Galactic γ-ray emission in the 1-100 MeV energy band may be due to inverse Compton scattering. It is also important in the central region of quasars.

3.2.2 Diffusion-loss equation for high-energy electrons

The *diffusion-loss equation* for the time evolution of the energy spectrum of CREs with particle density N(E) is given by (Longair, 2011):

$$\frac{\partial N(E,t)}{\partial t} = D\nabla^2 N(E,t) + \frac{\partial}{\partial E}[b(E)N(E,t)] + Q(E), \tag{3.16}$$

where D is the scalar diffusion coefficient, $b(E) = -(\mathrm{d}E/\mathrm{d}t)$ is the energy loss term given by the sum of all the five loss mechanisms mentioned in Sec. 3.2.1, and Q(E) describes the injection of high-energy electrons with an injection spectrum $Q(E) = \kappa E^{-p}$.

The form of b(E) for high-energy electrons under interstellar conditions is given by:

$$b(E) = -\left(\frac{\mathrm{d}E}{\mathrm{d}t}\right) = A_1\left(\ln\frac{E}{m_e c^2} + 19.8\right) + A_2 E + A_3 E^2. \tag{3.17}$$

The first term on the right-hand side, A_1, represents ionisation losses and depends only weakly upon energy; the second term, A_2, stands for bremsstrahlung losses and adiabatic losses and depends linearly on energy; and the last term, A_3, describes synchrotron and inverse Compton losses and depends on the square of the energy. It can be easily shown that if ionisation losses dominate, the energy spectrum flattens by one power of E, while if bremsstrahlung or adiabatic losses dominate, the spectrum remains unchanged, and lastly, if synchrotron or inverse Compton losses dominate, the spectrum steepens by one power of E.

Now, we solve Eq. 3.16 analytically, assuming that the diffusion term is negligible. The equation reduces to:

$$\begin{aligned} &\frac{\partial N(E,t)}{\partial t} = \frac{\partial}{\partial E}[b(E)N(E,t)] + Q(E), \\ \Rightarrow\ &\frac{\partial N(E,t)}{\partial t} = \frac{\mathrm{d}b(E)}{\mathrm{d}E}N(E,t) + b(E)\frac{\partial N(E,t)}{\partial E} + Q(E), \end{aligned} \tag{3.18}$$

which is a first-order partial differential equation solvable by the *method of characteristics*. We introduce help variables τ and ξ, such that

$$E = E(\tau,\xi), \qquad\qquad t = t(\tau,\xi).$$

Thus, we can write:

$$\begin{aligned} \frac{\mathrm{d}N}{\mathrm{d}\tau} &= \frac{\partial N}{\partial t}\frac{\mathrm{d}t}{\mathrm{d}\tau} + \frac{\partial N}{\partial E}\frac{\mathrm{d}E}{\mathrm{d}\tau}, \\ \Rightarrow \frac{\partial N}{\partial t}\frac{\mathrm{d}t}{\mathrm{d}\tau} &= \frac{\mathrm{d}N}{\mathrm{d}\tau} - \frac{\partial N}{\partial E}\frac{\mathrm{d}E}{\mathrm{d}\tau}. \end{aligned} \tag{3.19}$$

Comparing 3.18 and 3.19, we find three characteristic equations:

$$\frac{\mathrm{d}t}{\mathrm{d}\tau} = 1, \tag{3.20}$$

$$-\frac{\mathrm{d}E}{\mathrm{d}\tau} = b(E), \tag{3.21}$$

$$\frac{\mathrm{d}N}{\mathrm{d}\tau} = \frac{\mathrm{d}b(E)}{\mathrm{d}E}N + Q(E), \tag{3.22}$$

which are all ordinary differential equations. Using Eq. 3.20, we can rewrite Eq. 3.22 as:

$$\frac{\mathrm{d}N}{\mathrm{d}t} = \frac{\mathrm{d}b(E)}{\mathrm{d}E}N + Q(E). \tag{3.23}$$

Eq. 3.23 is an ordinary linear differential equation of the first order and has a standard solution given by:

$$N(E,t) = \exp\left(-\int \frac{\mathrm{d}b}{\mathrm{d}E}\mathrm{d}t\right)\left[\int Q \exp\left(\int \frac{\mathrm{d}b}{\mathrm{d}E}\mathrm{d}t\right)\mathrm{d}t\right] \tag{3.24}$$

Now, we assume that the losses are dominated by synchrotron and inverse Compton only, i.e., $b(E) = aE^2$ and that there is a single injection episode at $t = t_0$, with no subsequent injection of electrons, i.e., $Q(E) = \kappa E^{-p}\delta(t)$. Substituting Q and b in Eq. 3.24, we get:

$$N(E,t) = \kappa E^{-p} \exp\left[-2aE(t - t_0)\right]. \tag{3.25}$$

Fig. 3.3 shows a plot of Eq. 3.25. Using Eq. 3.2, we find the value of a, assuming B to be $10\,\mu$G. We observe that the cosmic ray electron spectrum evolves with time, *breaking* at higher energies first, and this break then migrates towards lower energies with time. This process of electron cooling, hence, gives rise to an *aged spectrum*. In our observations of dwarf galaxies, we find the break frequency by fitting such a model to our data, and hence, find the ages of the relativistic electrons (refer to Sec. 5.1.6).

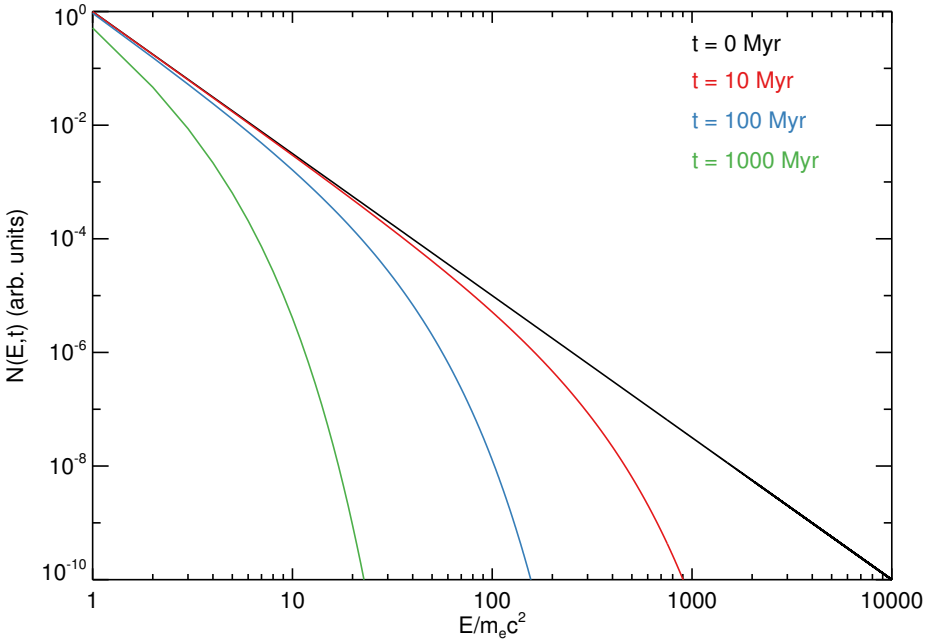

Fig. 3.3: Plot demonstrating electron cooling and spectral ageing

3.3 Diagnostic Tools to Detect Magnetic fields in the ISM/IGM

3.3.1 Synchrotron emission

Synchrotron emission provides a powerful tool to study cosmic magnetic fields, as it contains information about the total strength of the magnetic field. We shall now briefly discuss the physical quantities that can be deduced from measurements of synchrotron radiation. The following arguments can be applied to the synchrotron radiation emitted by the source at any frequency - radio, optical or X-ray wavelengths.

Suppose a source of synchrotron radiation with a volume V has luminosity L_ν at frequency ν. The spectrum of the radiation is of power-law form, $L_\nu \propto \nu^{-\alpha}$. The radio luminosity can be related to the energy spectrum of the cosmic ray electrons and the magnetic field B through the formula (Eq. 3.7) for synchrotron radiation:

$$L_\nu = A(\alpha) V \kappa B^{1+\alpha} \nu^{-\alpha}, \tag{3.26}$$

where the electron energy spectrum per unit volume is given by Eq. 3.6 and $A(\alpha)$ is a constant.

The total energy present in the source responsible for the radio emission is given by

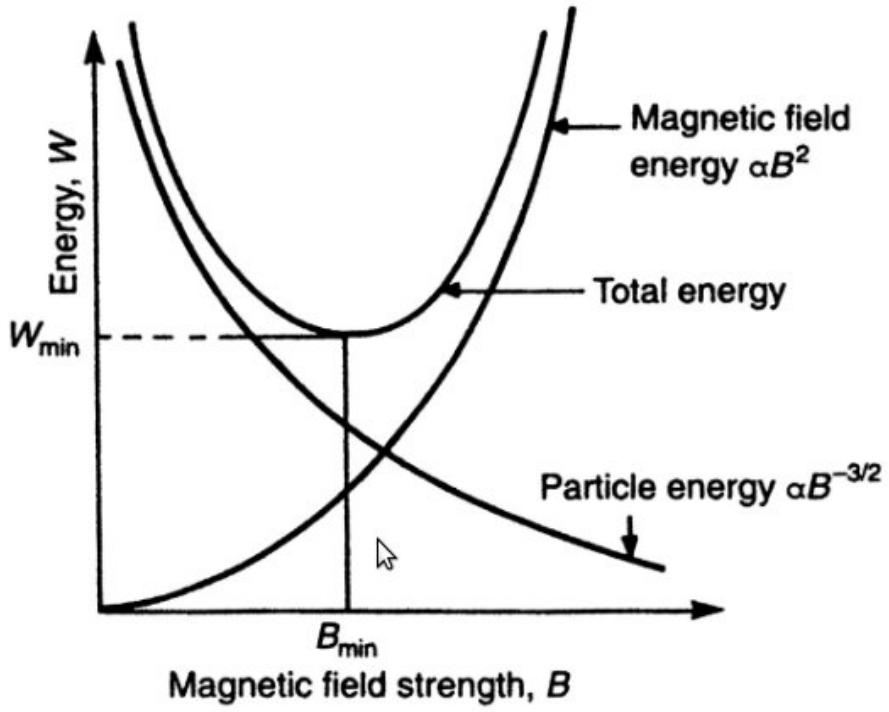

Fig. 3.4: Plot illustrating the origin of the minimum energy requirements of a radio source as a function of the magnetic field B. Taken from Longair (2011).

(Pacholczyk, 1970; Longair, 2011):

$$W_{total} = G(\alpha)\eta L_\nu B^{-3/2} + V\frac{B^2}{2\mu_0}, \tag{3.27}$$

$$G(\alpha) = \eta\frac{V}{p-2}\frac{C}{A(\alpha)}\nu^\alpha\left(\nu_{min}^{(2-p)/2} - \nu_{max}^{(2-p)/2}\right), \tag{3.28}$$

$$C = 0.29\left[\frac{3}{2}\frac{q_e}{(m_e c^2)^3}\right], \tag{3.29}$$

where C results from the assumption that the maximum intensity of synchrotron radiation occurs at a frequency $\nu = 0.29\nu_c$, where ν_c is the critical frequency given by Eq. 3.5. η accounts for cosmic ray protons.

The variations of the energies in particles with the magnetic field are shown in Fig. 3.4. There is a minimum total energy which can be found by minimising Eq. 3.27 with respect to B,

$$B_{min} = \left[\frac{3\mu_0}{2}\frac{G(\alpha)\eta L_\nu}{V}\right]^{2/7}. \tag{3.30}$$

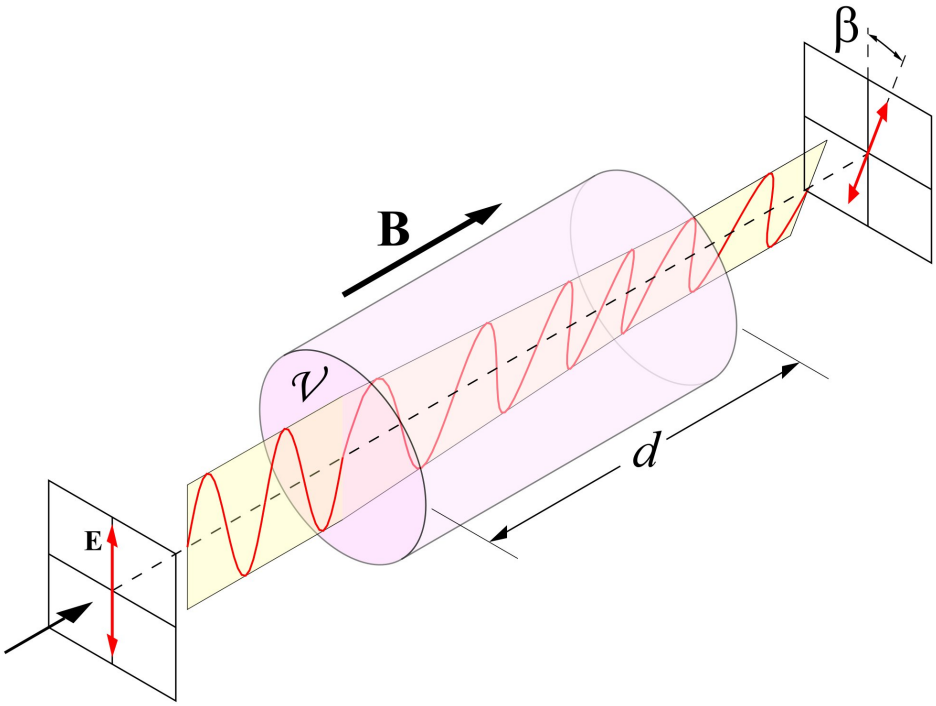

Fig. 3.5: Polarization rotation due to the Faraday effect.

Substituting B_{min} in Eq. 3.27 , we get:

$$W_{mag} = \frac{3}{4} W_{particles}. \tag{3.31}$$

Thus, the minimum energy requirement corresponds closely to what is often referred to as *equipartition*. These results can be used in our studies, but with a few limitations in mind. There is no physical justification for the cosmic ray particle energy and the magnetic field energy being close to equipartition. However, although imprecise, this method gives a reasonable estimation of the B field strength. Furthermore, the magnetic field estimate weakly depends on η, which is highly uncertain in many contexts. For sufficiently steep spectra, the estimate depends on the minimum energy of CRe assumed, which corresponds usually to the minimum frequency observed. Moreover, the volume is a priori unknown and represents the largest uncertainty. To address these issues, a revised formalism has been proposed by Beck & Krause (2005), which is what has been used in our work (Sec. 5.1.5).

3.3.2 Faraday rotation

Electromagnetic waves propagating through a magnetised plasma experience an effect called *Faraday rotation*, which essentially results in the right and left-circular polarisation states travelling with different phase velocities. For a linearly polarised wave, which can be seen as the superposition of a right and a left-circularly polarized beam, this results in a rotation with time (or path length) of the electric field vector by an angle given by

(Widrow, 2002):

$$\varphi = \frac{e^3\lambda^2}{2\pi m_e^2 c^4} \int_0^{l_s} n_e(l) B_\parallel(l) \mathrm{d}l + \varphi_0, \tag{3.32}$$

where λ is the radiation wavelength, $n_e(l)$ is the density of thermal electrons along the line-of-sight from the source ($l = l_s$) to the observer ($l = 0$), $B_\parallel$ is the line-of-sight component of the magnetic field, and φ_0 is the initial polarisation angle. Fig. 3.5 illustrates the the Faraday effect (φ is shown as β in the figure). Faraday rotation yields information about the line-of-sight component of the magnetic field *and its direction*.

Rotation measure

The Faraday rotation angle φ is written usually in terms of the *rotation measure*, RM:

$$\varphi = (RM)\lambda^2 + \varphi_0, \tag{3.33}$$

$$\begin{aligned} RM &\equiv \frac{e^3}{2\pi m_e^2 c^4} \int_0^{l_s} n_e(l) B_\parallel(l) \mathrm{d}l \\ &\simeq 810 \int_0^{l_s} \left(\frac{n_e}{\mathrm{cm}^{-3}}\right) \left(\frac{B_\parallel}{\mu\mathrm{G}}\right) \left(\frac{\mathrm{d}l}{\mathrm{kpc}}\right) \ \mathrm{rad\,m}^{-2} \end{aligned} \tag{3.34}$$

It is difficult to determine RM unambiguously, since one cannot distinguish between φ and $\varphi \pm n\pi$. This is called the $n\pi$ *degeneracy* and can be removed by measuring φ at three or more wavelengths.

Depolarisation

In addition to the rotation of the plane of polarisation (given by φ above), we are interested in the *degree of polarisation* given by Eq. 3.10. This degree of polarisation depends only weakly on frequency. However, it never reaches its maximum, due to a number of effects, commonly referred to as *depolarisation*. Burn (1966) discusses this depolarisation effect extensively.

An instrumental effect that reduces the degree of polarisation is the so-called *bandwidth depolarisation*. The reason for this is that the polarisation angle rotates across the bandwidth of observation. At low radio frequencies, bandwidth depolarisation can be very strong, and the best way to overcome this is by splitting the band into many sub-bands and applying the RM synthesis technique, discussed in the next section (Sec. 3.3.2).

Another effect is the *beam depolarisation*. Imagine looking at a non-uniformly polarised, extended source, with a radio telescope whose resolution is poorer than the angular scale over which the source polarisation is coherent. Then, in any given resolution element, there would be regions with different polarisation characteristics. Thus, the beam would smooth out the polarisation of the source, and the measured polarisation

would be less than the true source polarisation. Beam depolarisation cannot in principle be corrected for. The only way to obtain the true source polarisation is to observe with sufficiently high angular resolution, that is using the long baselines.

Both the above two effects are induced externally. There can be a third depolarisation effect internal to the source itself, known as the *internal Faraday depolarisation*. This is due to the spatial extent of the source itself and occurs even if the intervening media are completely homogeneous. Along the line of sight, the emission from individual electrons within a source arises from different depths and suffers different Faraday rotation angles due to the different path lengths. For the total radiation emitted by the source, this results in a reduction of the observed degree of polarisation.

RM synthesis

Traditionally, RM is determined by plotting the observed polarisation angle as a function of the square of the observing wavelength, and performing a least-squares fit to the data. As discussed concisely by Heald (2009), there are three potential problems with this approach:

- The $n\pi$ *degeneracy*, already mentioned in Sec. 3.3.2.
- Polarized emission with different RM values can be present in a single line of sight. The signal from these different regions mixes, and makes a linear fit inappropriate.
- Faint sources with high RM will be undetectable in individual channels due to low signal-to-noise, and will remain undetectable even after integrating all channels due to bandwidth depolarization (mentioned in Sec. 3.3.2). Thus, no data points would be available for a traditional linear fit. At low radio frequencies, bandwidth depolarisation is strong enough to totally cancel any polarisation signal.

In order to deal with these problems, a novel technique was introduced by Burn (1966), and recently extended and implemented by Brentjens & de Bruyn (2005), who coined the term *RM synthesis* to describe it. For a complete mathematical treatment, which is out of the scope of this thesis, the reader is requested to refer to the aforementioned works.

Bandwidth depolarisation is the cardinal problem circumvented by RM synthesis. Since this technique is easily applied to wide fields, one can conduct very fast RM surveys of weak sources. Also, multiple sources along the line of sight, can be easily detected. Under certain conditions, it is even possible to recover the emission as a function of Faraday depth within a single cloud of ionized gas.

Chapter 4

Observations and Data Reduction

4.1 Observations with the WSRT at 92 cm

We observed the radio continuum emission from starburst dwarf galaxies NGC 1569 and NGC 4449 at 92 cm, with the Westerbork Synthesis Radio Telescope (WSRT). This telescope is an east-west inteferometer which comprises fourteen 25 m antennae and uses the earth's rotation to fully synthesize the UV-plane. Ten of the dishes (labelled 0 - 9) are on fixed, equatorial mountings, 144 m apart from each other, while the remaining four (2×2) dishes (labelled A, B, C, D) are movable along two east-west tracks. In the array, the baselines can extend from 36 m to 2.7 km.

The observations were done as a part of the project R11A/002 (PI: U. Klein) on November 13, 2010 (NGC 1569) and May 11, 2011 (NGC 4449). They consisted of one 12-hours run (for each galaxy) with the *maxi-short configuration*, which uses an RT9-RTA separation of 36 m, an RTA-RTB separation of 54 m, and an RTC-RTD separation of 72 m. *The short baselines from this configuration (36 m, 54 m, 72 m and 90 m) are identical to those from a traditional* 4×12 *hour coverage.* Although the overall sidelobe levels are not as low, image fidelity in the reconstructions of very extended sources is comparable [1]. Figure 4.1 shows the UV coverage of NGC 1569 in a single channel of a single sub-band.

The 92 cm feeds/receivers span the frequency range of about 315-385 MHz. The wide-band correlator can independently process 8 tunable bands of 10 MHz centred at roughly 320, 329, 338, 346, 355, 364, 373, and 381 MHz. For this frequency range, the WSRT is equipped with linearly polarized feeds. The "x dipole" is oriented in the north-south direction and the "y dipole" in the east-west. Each band is sub-divided into 128 channels in all four cross- correlations to recover all Stokes parameters, with an integration time of 60 seconds. For our observational setting, the largest angular scales detectable by WSRT is approximately 1.5°, which is much larger than the size of both the galaxies. Hence, there is very little chance that large-scale emission from the galaxies are resolved out at this wavelength, i.e., the problem of *missing short-spacings* is negligible. The maximum spatial resolution of the WSRT at this wavelength is 55″ in the East-West direction and 110″ in the North-South direction. For our observations of NGC 1569, the synthesized beam size is $47\farcs21 \times 41\farcs74$, and that of NGC 4449 is $50\farcs11 \times 35\farcs89$.

For such observations with the WSRT, usually two pairs of calibrator are observed, one pair before and one after the target source, each pair consisting of one polarised and one unpolarised source. For NGC 4449, 3C 147 and the eastern hotspot of DA 240 were

[1] Refer to: www.astron.nl

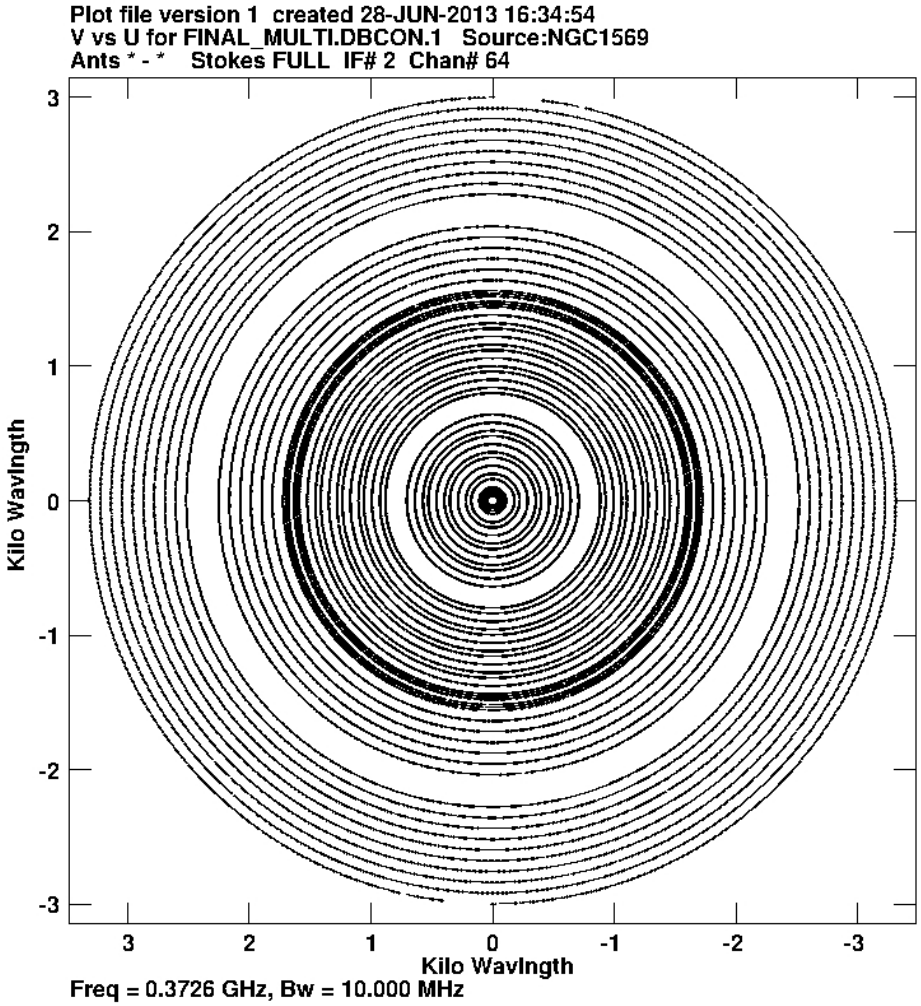

Fig. 4.1: UV coverage of NGC 1569

observed before NGC 4449, and 3C 409 and PSR 1937 + 21 afterwards. However, for reasons unknown, the operator did not observe polarized calibrators along with NGC 1569. Instead, two unpolarised calibrators – 3C 48 before the target and 3C 286 after – were observed. Hence, we had to obtain polarised calibrators DA 240 and 3C 303 from a different observation of a different project target, made 5 days later, with exactly similar settings.

Table 4.1 gives a summary of the observations.

4.2 Data reduction method

Both the datasets were first loaded into the Astronomical Image Processing System (AIPS) package, version 31DEC12. AIPS, which is tailored to the VLA telescope data, can normally handle only circular polarised feeds. Hence, the UV data headers need to be redefined to circular polarisation while working in AIPS, and can be changed back to linear later. First the system temperatures were applied. Since this dataset had large

Parameter	NGC 1569	NGC 4449
Wavelenth (cm)	92	92
Array configuration	maxi-short	maxi-short
Bandwith per IF (MHz)	10	10
Channels per sub-band	128	128
IF1 (MHz)	381.3	381.4
IF2 (MHz)	372.6	372.6
IF3 (MHz)	363.8	363.9
IF4 (MHz)	355.1	355.2
IF5 (MHz)	346.3	346.4
IF6 (MHz)	337.6	337.6
IF7 (MHz)	328.8	328.9
IF8 (MHz)	320.1	320.2
Flux/Bandpass calibrator	3C 48	3C 147
Instrumental polarization calibrator	3C 48	3C 147
Absolute polarization angle calibrator	DA 240	DA 240

Tab. 4.1: Summary of WSRT 92 cm Observations

amounts of Radio Frequency Interference (RFI), we decided to try out the automatic flagger called RFI console (Offringa et al., 2010). The RFI console, with it's graphical frontend RFI GUI, was successfully used by Adebahr et al. (2013), on their WSRT data of M 82 at 92 cm. A unique flagging strategy was developed for each of the sources. This initial flagging removed most of the large scale RFI. The data were loaded back in AIPS, and the remaining RFI were removed manually, using the task SPFLG, one baseline and one stokes at a time.

After the flagging was complete, a bandpass calibration was applied to both the datasets. Next, the NGC 1569 data were flux-calibrated using 3C 48, and the NGC 4449 data using 3C 147. The flux scale used by the SETJY task in AIPS for 3C 48 is "(1999.2) VLA", and for 3C 147 is "(2010) VLA". At frequency 355 MHz, the flux value of the former is 41.2585 Jy and that of the latter 44.9936 Jy. For the polarisation calibration, another novel technique was used, which will be discussed in Section 4.3.

For self-calibration and imaging in total power, we exported the data to the MIRIAD package (version 3.1). The East-West configuration of the WSRT (which means, redundant baselines) and the observational setting, with one calibrator in the beginning and one at the end, make self-calibration a very significant step in the data reduction, for high-dynamic-range images (Adebahr et al., 2013). Self-calibration is applied to remove residual phase and gain variations. This was done for each of the eight sub-bands independently, using *masks* during the "clean" step, in order to include all diffuse emission in the field. There were *five* phase-only selfcal cycles needed, each time reducing the "interval" parameter of the "selfcal" task. Consequently, the values (in minutes) of "interval" used were 20, 10, 5, 3 and 1. The 6th and last cycle was an amplitude-only cycle. The eight separate images were then combined and primary beam corrected.

The theoretical continuum image noise of a 12 h observation at 350 MHz, combining all the 8 sub-bands is 0.1375 mJy/beam (uniform weighting). However, the total intensity

map is confusion limited at 0.3 mJy/beam. The final noise level in the total power image of NGC 1569 is ≈ 0.3 mJy/beam, and in that of NGC 4449 is ≈ 0.5 mJy/beam.

4.3 Polarization calibration technique

As part of the project goals, we wanted polarisation images as well. The standard AIPS tasks did not suffice, because at such low frequencies, the Stokes Q and U might vary significantly over the entire frequency range, even over the bandwidth of one sub-band. This would result in an erroneous model for some channels in a sub-band. Hence, the whole process of calibration, self-calibration and imaging were done for each channel separately, as described by de Bruyn & Brentjens (2005).

The whole calibration was done in CASA (version 3.3.0), using a script. Calibrator gains and polarisation leakage terms were determined from the unpolarised calibrators, while the polarisation angle terms were determined from the polarised calibrators. The model parameters for each calibrator were defined from a fourth order polynomial with coefficients *A, B, C,* and *D*, as described in the VLA Calibrator Manual [2]. Also, the polarised calibrator models were given values of a fractional polarisation, an intrinsic polarisation angle and a rotation measure. The fluxes in all the four cross-correlations were then calculated, for each individual channel.

After this, self-calibration and imaging were done, for each Stokes separately, much like the process described for total power in the previous section, but for each channel this time. Masks from the total power self-calibration were used to include all diffuse emission in the model. The final cycle used an amplitude and phase calibration with a solution interval of one minute. The final images were cleaned to three times the noise level and primary beam corrected. Next, all the final images were checked by eye, for significant calibration errors and residual RFI. Images with significant artifacts and noise level three times higher than the average were discarded.

[2] http://www.vla.nrao.edu/astro/calib/manual/baars.html

Chapter 5

Analysis and Results

5.1 NGC 1569

5.1.1 Total intensity and morphology

We have detected radio continuum emission from NGC 1569 at $\lambda 92$ cm. Figure 5.1 shows the total power image contours, overlaid on a colour image of the Hα map by Hunter & Elmegreen (2004). The beam size of the radio map is $47''.21 \times 41''.74$. From the map, we obtain a total flux density of 750 ± 20 mJy (3σ). The RMS in the image is 0.3 mJy/beam.

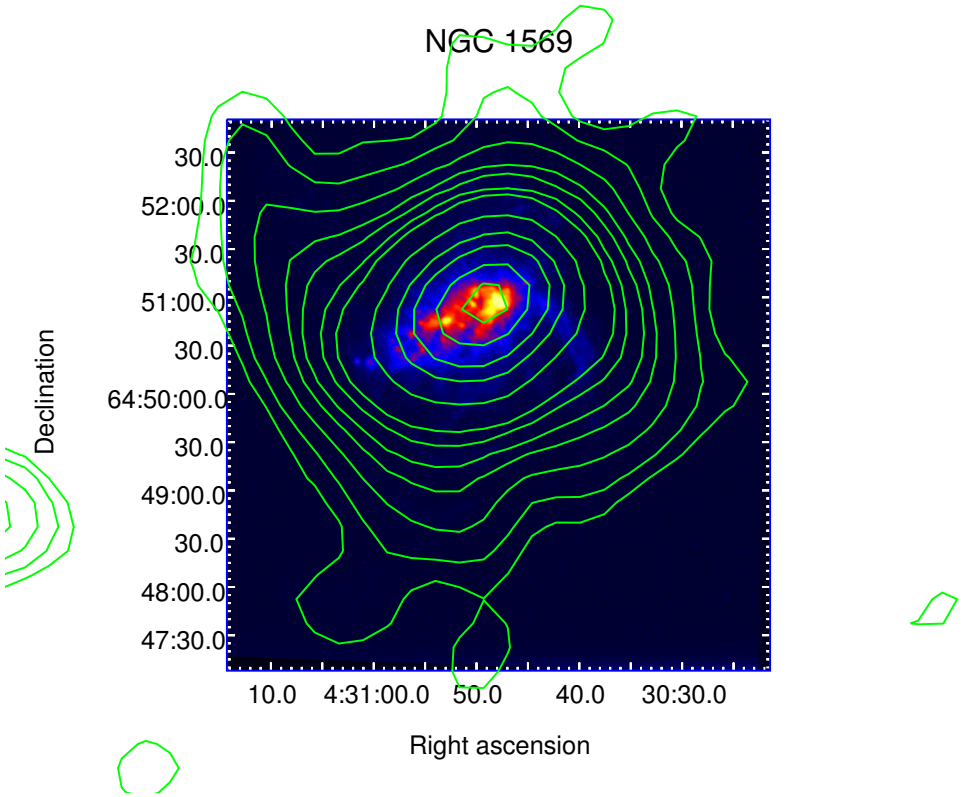

Fig. 5.1: Radio continuum contours of NGC 1569 at $\lambda 92$ cm (WSRT), overlaid on a colour image of the Hα map by Hunter & Elmegreen (2004). Contours start at a 3σ level of 0.001 Jy/beam, and then increase as 0.002, 0.004, 0.007, 0.01, 0.015, 0.02, 0.04, 0.07, 0.1, 0.15 and 0.2 in unit of Jy/beam.

The galaxy has a *boxy* structure, which is reminiscent of the morphology seen in X-rays and Hα. Assuming an inclination of 63° (Stil & Israel, 2002), the maximum physical extent of the galaxy is 16.5 kpc. The scale length of the galaxy is 744 pc, nearly two times the value at 20 cm reported by Kepley et al. (2010).

5.1.2 Integrated radio continuum spectrum

The total intensity of the radio continuum emission from a source contains information about the combined free-free (thermal) and non-thermal emission. By separating the two kinds of emission, one can arrive at an estimation of the total magnetic field strength. One can adopt different techniques to separate the thermal and the non-thermal emission. We obtained total flux density values available in the literature at different radio frequencies and also added the new value from our observation at 350 MHz to the repository. Table 5.1 lists all the flux density values used along with the references. For the data points which have more than one literature reference, an average value has been used. For the decomposition of the spectrum into the thermal and non-thermal compo-

Frequency (GHz)	Flux density (mJy)	References
0.350	750 ± 20	1
0.610	610 ± 20	2
1.415	425 ± 20	2,3
2.700	318 ± 20	4,5
4.800	233 ± 20	6,7,8
8.350	176 ± 5	9
10.700	155 ± 10	6
15.360	116 ± 13	10
24.500	96 ± 8	6

Tab. 5.1: NGC 1569: Integrated flux densities at different radio frequencies. References: (1) This work, (2) Israel & de Bruyn (1988), (3) Hummel (1980), (4) Pfleiderer et al. (1980), (5) Sulentic (1976), (6) Klein & Gräve (1986), (7) Gregory & Condon (1991), (8) Becker et al. (1991), (9) Effelsberg, unpublished (Klein), (10) Lisenfeld et al. (2004).

nents, we assumed only that the free-free spectrum has a slope $\alpha_{th} = -0.1$. The resulting free-free flux density at 1 GHz, 111 mJy, is close to previous estimates (Israel & de Bruyn, 1988; Lisenfeld et al., 2004). The non-thermal spectrum was fitted to a power-law with an exponential cut-off, which is consistent with a single burst injection spectrum, taking into account only synchrotron and inverse Compton losses (as discussed in Sec. 3.2.2). Figure 5.2 shows the resulting spectrum. The fitted non-thermal spectrum exhibits a cut-off frequency at $\nu_b = 12.4 \pm 2.0$ GHz.

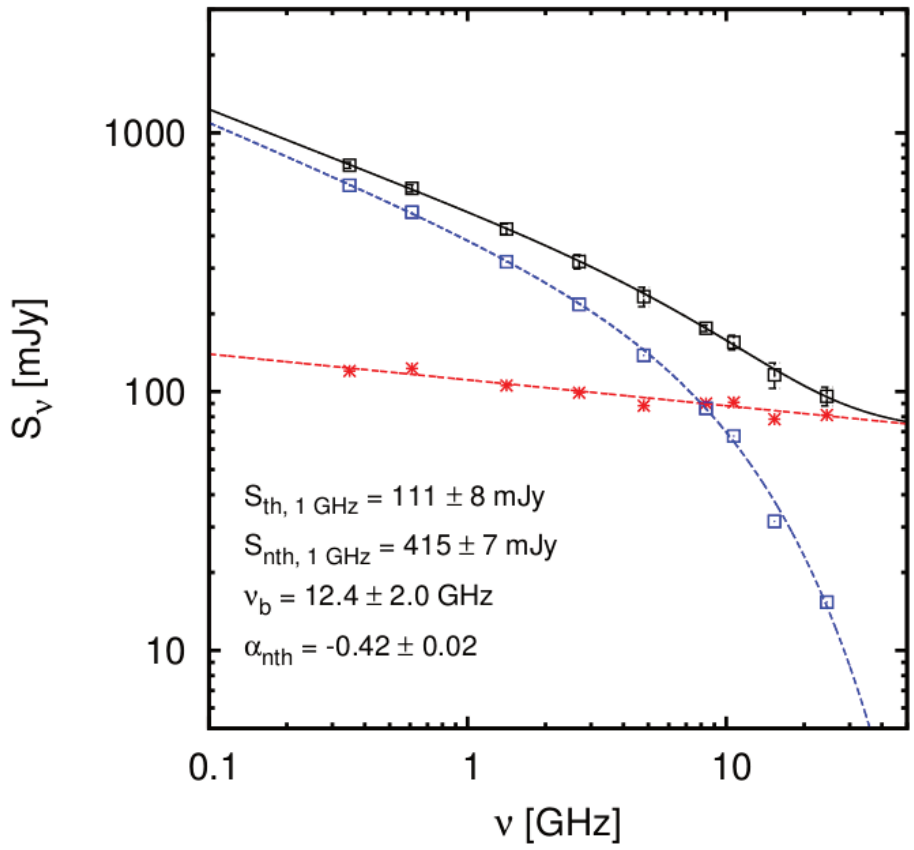

Fig. 5.2: Integrated radio continuum spectrum of NGC 1569, with the fitted total average flux densities (red squares), the free-free radiation (green crosses), and the synchrotron fluxes (blue stars), the latter obtained by subtracting the thermal from the total fluxes.

5.1.3 Spectral index

In order to map the radial evolution of the break in the synchrotron spectrum, we obtained total power maps at different frequencies. Other than our new map at 350 MHz, we had at our disposal *four* other maps from the work of Kepley et al. (2010) - 1.4 GHz, 2.3 GHz, 4.9 GHz and 8.5 GHz. All these maps were smoothed to the lowest resolution, that of the 350 MHz map ($47\farcs21 \times 41\farcs74$). We now used a map of the Hα emission from the galaxy (Hunter & Elmegreen, 2004) to estimate the thermal (free-free) component of the radio emission. For this, we scaled the Hα map to the thermal flux density value at 1 GHz obtained from the fit (Figure 5.2). Using this scaled map, we obtained maps of thermal emission at all the five frequencies, and subtracted them from the total intensity maps, to finally obtain five maps of non-thermal emission. Thereafter, a spectral index map (Figure 5.3) between the five frequencies was obtained by using the tasks MCUBE, TRANS and SPIXR in AIPS. Non-thermal spectral indices vary between 0.41 at the core up to 0.85 near the edges. Such flat spectra at the core are observed in a dwarf galaxy for the first time. This might point towards *non-linear diffusive shock acceleration* (Brunetti, priv. comm, discussed in Sec. 6.1).

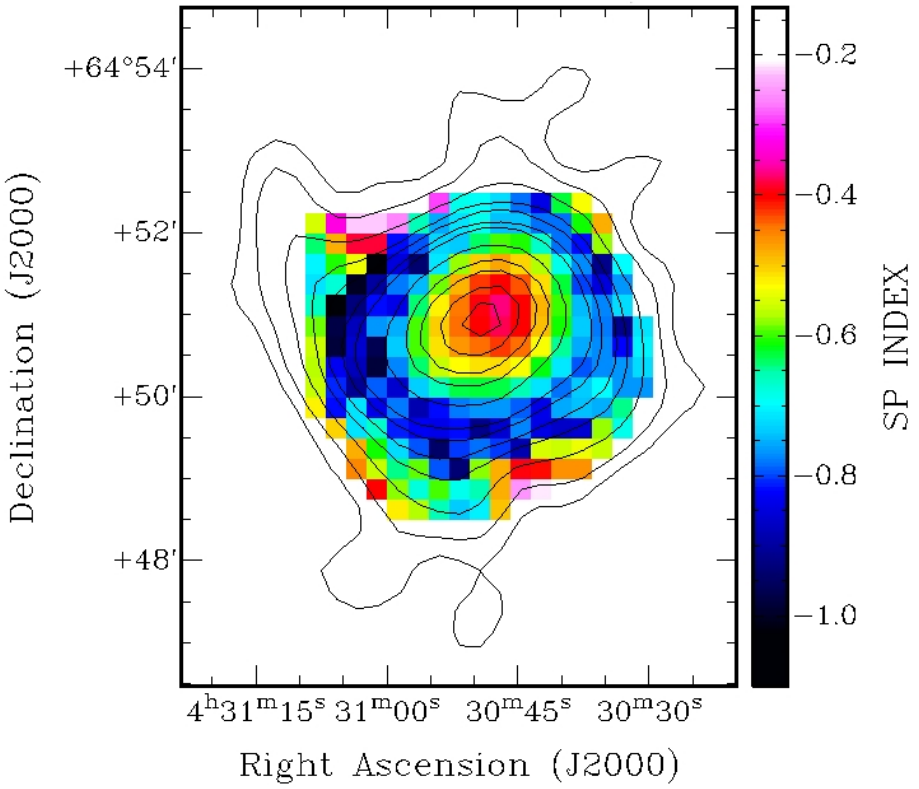

Fig. 5.3: Spectral index colour-map of NGC 1569 between 350 MHz, 1.4 GHz, 2.3 GHz, 4.9 GHz and 8.5 GHz. The colour-bar is in linear scale. Overlaid are the contours of the total power map at 350 MHz, same as in Figure 5.1.

5.1.4 Radial evolution of the break

We now used the task IRING in AIPS, to radially average the non-thermal intensities in each map, in elliptical bins. The width of each bin was taken as 40″, since the width should be atleast as large as the beam size, to ensure that we use uncorrelated data. We did an exhaustive error-analysis, to find the error in the intensities in all the maps. The rms in 5-6 different off-source regions in the map were read and the mean of that, σ_{noise}, was calculated. Additionally, the mean intensity in the same regions were also read and the standard deviation of the mean intensities, σ_{base}, was calculated. The error in the intensities in each ring was then given by:

$$\sigma_{total} = \frac{1}{\sqrt{N}} \cdot \sigma_{noise} + N \cdot \sigma_{base}, \tag{5.1}$$

where N is the number of beams in each bin. The details of the error-analysis of each map can be found in Appendix A. Now, we collected the intensity values at each radius and fitted them to our exponential-cutoff model (same as in Sec. 5.1.2). The resulting

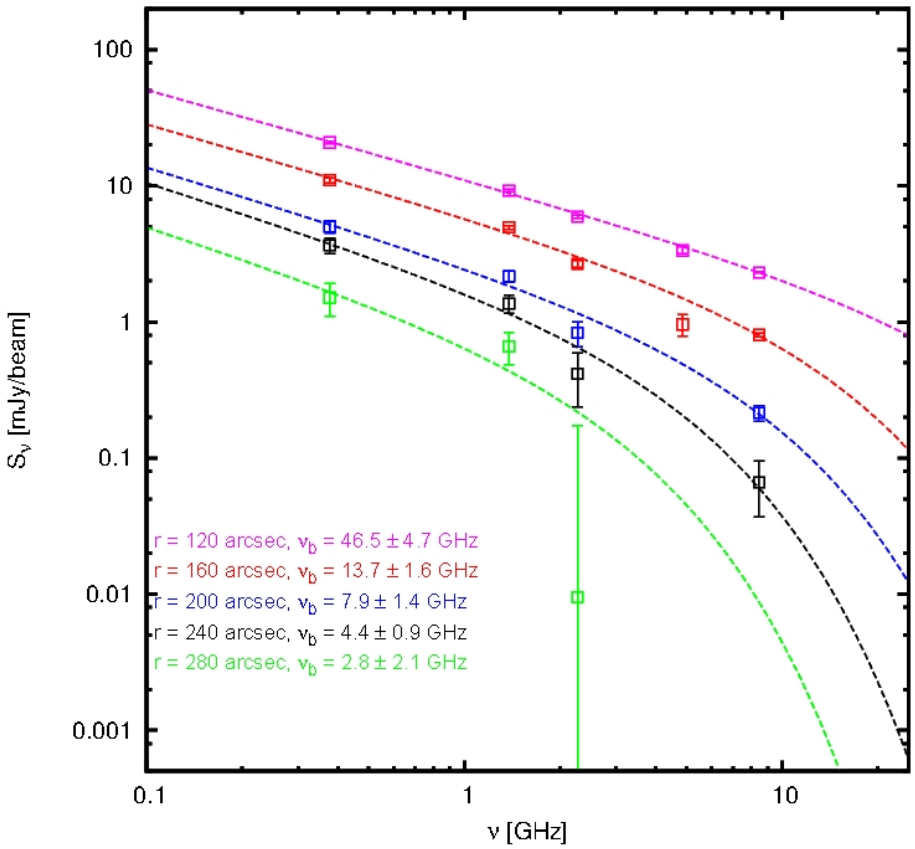

Fig. 5.4: Migration of the break frequency of NGC 1569 towards lower values with increasing radius. For the last radius at 280″, there were only three points available. Hence, the spectral index parameter was fixed at a value of -0.75, and the spectrum fitted with two free parameters.

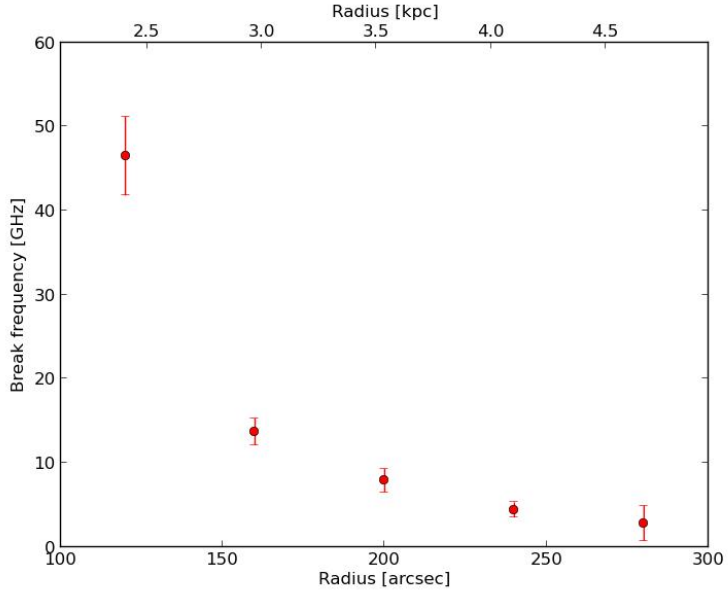

Fig. 5.5: NGC 1569: Plot of break frequency with errors against radius, clearly showing the decreasing trend.

plot is shown in Figure 5.4. The plot shows that the break, indeed, migrates towards lower frequencies. As discussed in Sec. 3.2.2, physically this translates into the process of spectral ageing, i.e., cooling of the cosmic ray electrons as they travel outwards from the galaxy. At the outer radii, we are essentially looking at *older* electrons, and can find their ages since the supernova explosion (Sec. 5.1.6). We show a plot of the break frequencies versus radius in Figure. 5.5.

The errors in the break frequencies resulting from the three-parameter-fit have been *marginalised* by doing a re-fit via only the break-frequency parameter, while keeping the other two parameters fixed at the best-fit values. This process of marginalising the errors (refer to Chap. 15 in Press et al. 1992) is justified because the correlation matrix given by the fitting routine showed very high values (close to 1.0) of the off-diagonal elements, which means that the parameters are highly correlated and the error of one propagates considerably into the other. Therefore, the error in the break frequency can not be reliably estimated without marginalisation.

5.1.5 Equipartition magnetic field strength

We estimate the equipartition magnetic field strength (Sec. 3.3.1), using the revised equipartition formula proposed by Beck & Krause (2005). The non-thermal intensities at $\lambda 92\,\mathrm{cm}$ (350 MHz) have been used for the entire computation. We assumed a spherical geometry for the synchrotron-emitting medium, and calculated the path-length at every pixel. The number density ratio of protons to electrons was assumed to be 100 (Beck, priv. comm). The spectral index map in Figure 5.3 was used for the spectral index at every pixel. Since this formalism has a requirement that all the spectral indices be steeper than -0.5, we replaced the flatter values in the map with -0.51. This might lead to an over-estimation of the equipartition magnetic field in the core of the galaxy. The map resulting from our computations is shown in Figure 5.6. Overlaid are the contours of non-thermal intensities at $\lambda 92\,\mathrm{cm}$. Average equipartition magnetic field strength over the whole galaxy turns out to be $\approx 10\,\mu\mathrm{G}$. The average value at the core is $\approx 30\,\mu\mathrm{G}$ and the average value in the halo is $\approx 8\,\mu\mathrm{G}$, both of which are consistent with the total equipartition magnetic field strength values estimated by Kepley et al. (2010).

The errors in the magnetic field strength are estimated numerically using a *Monte Carlo approach*. Essentially, the error in the spectral index is assumed to be Gaussian random. The best estimate and the error in the spectral index from the earlier fit (Figure 5.4) are then used to generate 1024 random realizations of the spectral index, and the equipartition magnetic field strength is derived for each of the realizations. The resulting distribution of the magnetic field from the simulation is found to be symmetric, and can be closely approximated as a Gaussian. The mean and standard deviation of this Gaussian distribution are hence taken as the best estimate of the magnetic field strength and its error, respectively.

5.1.6 Spectral ages and wind velocity

We can now calculate the ages of the relativistic electrons, that have travelled away from the galaxy. Assuming only synchrotron and inverse Compton losses, the spectral age is

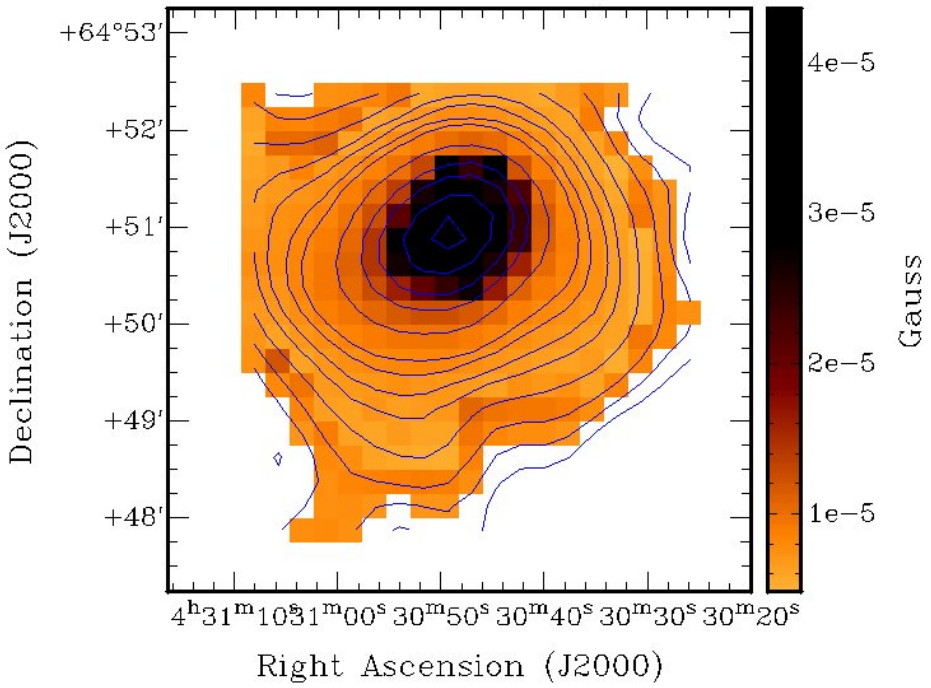

Fig. 5.6: Colour image of the total equipartition magnetic field strength estimated in NGC 1569. The colour-bar is linear. Overlaid are the contours of the non-thermal intensity at $\lambda 92\,\mathrm{cm}$.

given by:

$$t_{spec} = 1.59 \cdot 10^9 \cdot \frac{B_{eq}^{1/2}}{B_{eq}^2 + B_{rad}^2} \left[\left(\frac{\nu_b}{\mathrm{GHz}} \right) (1+z) \right]^{-1/2} \mathrm{yr}, \tag{5.2}$$

where B_{eq} is the equipartition magnetic field strength, ν_b is the break frequency, z is the red-shift and B_{rad} is the equivalent magnetic field strength of the radiation field of the galaxy. The energy density of the radiation field, $U_{rad} = B_{rad}^2/8\pi$, can be estimated from the bolometric luminosity of the galaxy to be $3.6\,\mathrm{eV\,cm^{-3}}$(Lisenfeld et al., 2004). Ages at the five radii are calculated using ν_b values from Figure 5.4 and B_{eq} values from Figure 5.6. The errors in the ages are numerically estimated using the errors in ν_b and B_{eq} with the same Monte Carlo approach as used in Sec. 5.1.5.

Figure 5.7 shows the radial profile of the spectral ages of NGC 1569. From the linear fit, a *wind velocity* $\approx 255 \pm 12\,\mathrm{km\,s^{-1}}$ was calculated. The escape velocity of NGC 1569 is small, i.e. in the range $50 - 100\,\mathrm{km\,s^{-1}}$ (Heckman et al., 1995; Devost et al., 1997). This wind velocity is almost three times the escape velocity, which indicates that the

cosmic rays and magnetic fields can be ejected out and can possibly pollute the IGM (discussed in Sec. 6.1). Table 5.2 summarises the main results of our analysis of NGC 1569.

5.1.7 RM synthesis

The Stokes Q and U images obtained after calibration and imaging, as described in Sec. 4.3, were run through a basic RM Synthesis code (Sec. 3.3.2). However, there was no believable polarisation detected. The low galactic latitude of NGC 1569 (11.2°) might be a reason any possible weak emission is being depolarised by the strong Galactic foreground.

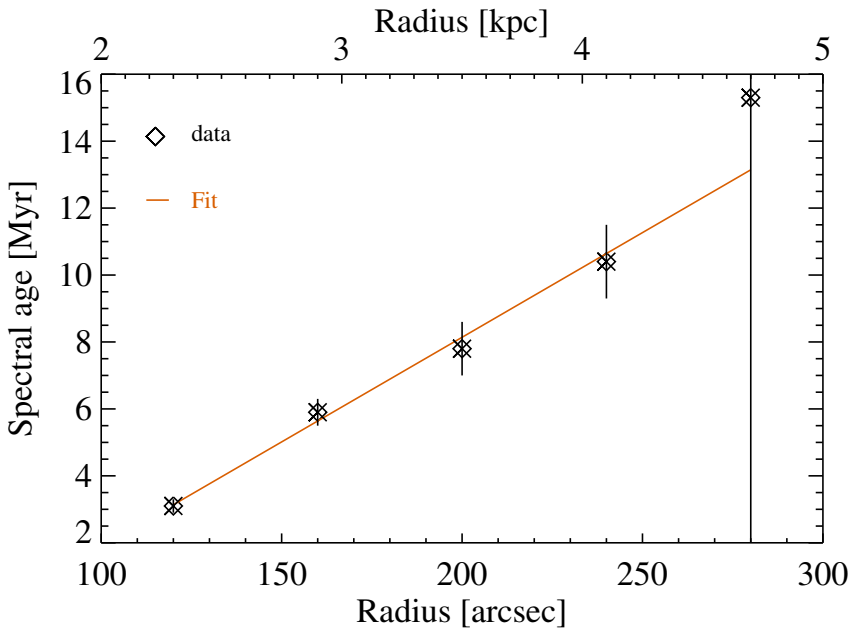

Fig. 5.7: NGC 1569: Plot of the estimated spectral ages with errors against radius. The fit is linear and the wind velocity is estimated from the slope.

r (arcsec)	r (kpc)	I_ν (Jy/beam)	α_{nth} -	ν_b (GHz)	B_{eq} (μG)	t_{spec} (Myr)
120	2.1	0.0207	-0.656 ± 0.0083	46.5 ± 4.7	8.8 ± 0.06	3.1 ± 0.2
160	2.8	0.0109	-0.667 ± 0.0327	13.7 ± 1.6	7.4 ± 0.20	5.9 ± 0.4
200	3.5	0.0050	-0.701 ± 0.0745	7.9 ± 1.4	6.1 ± 0.84	7.8 ± 0.8
240	4.2	0.0037	-0.730 ± 0.1019	4.3 ± 0.9	5.7 ± 0.37	10.4 ± 1.1
280	5.0	0.0015	-0.750 (fixed)	2.8 ± 2.1	4.4 ± 0.00	15.3 ± 16.8

Tab. 5.2: NGC 1569: Results at a glance - r is the galactocentric distance, I_ν is the intensity at $\lambda 92\,\mathrm{cm}$, α_{nth} is the non-thermal spectral index, ν_b is the break frequency, B_{eq} is the equipartition magnetic field strength and t_{spec} is the spectral age.

5.2 NGC 4449

The analysis of NGC 4449 is done exactly in the same line as NGC 1569, and the results are presented in the following sections.

5.2.1 Total intensity and morphology

We have detected radio continuum emission from NGC 4449 at $\lambda 92$ cm. Figure 5.8 shows the total power image contours, overlaid on a colour image of the Hα map by Bomans et al. (1997). From the map, we obtain a total flux density of 514 ± 21 mJy (3σ). The RMS is 0.5 mJy/beam. The beam size of the radio map is $50\farcs11 \times 35\farcs89$. The galaxy at $\lambda 92$ cm shows a morphology very similar to that at $\lambda 49$ cm (Klein et al., 1996). Assuming an inclination of 68° (Hunter et al., 2002), the maximum physical extent of the galaxy is 22.1 kpc . The scale length of the galaxy is 1.1 kpc, which is *not* larger than the scale length of 1.3 kpc from the map of Klein et al. (1996) at $\lambda 49$ cm.

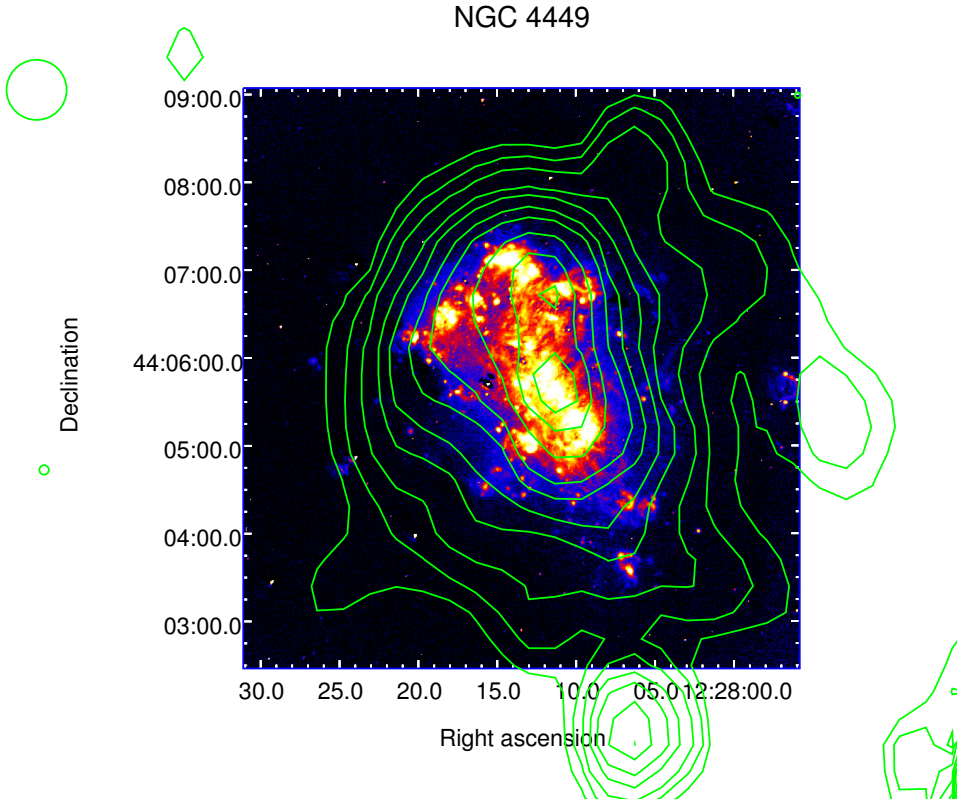

Fig. 5.8: Radio continuum contours of NGC 4449 at $\lambda 92$ cm (WSRT), overlaid on a colour image of the Hα map by Bomans et al. (1997). Contours start at a 3σ level of 0.0015 Jy/beam, and increase as 0.0025, 0.004, 0.007, 0.01, 0.015, 0.02, 0.03, 0.04 and 0.048 in unit of Jy/beam.

5.2.2 Integrated radio continuum spectrum

Table 5.3 lists all the flux density values used for NGC 4449 along with the references. For the data points which have more than one literature reference, an average value has been used.

Figure 5.9 shows the resulting spectrum. The fitted non-thermal spectrum exhibits a cut-off frequency at $\nu_b = 5.2 \pm 1.3\,\mathrm{GHz}$, much lower than for NGC 1569.

Frequency (GHz)	Flux density (mJy)	References
0.327	501 ± 20	1
0.350	514 ± 21	2
0.609	450 ± 40	3
1.490	278 ± 15	4,5
2.695	204 ± 12	6
4.875	137 ± 9	7,8
10.650	87 ± 5	7,9,10
24.500	67 ± 10	7

Tab. 5.3: NGC 4449: Integrated flux densities at different radio frequencies. References: (1) WENSS, Klein et al. (in prep.), (2) This work, (3) Klein et al. (1996)(recomputed), (4) NVSS, Klein et al. (in prep.), (5) Condon (1987), (6) Klein et al. (in prep.), (7) Klein & Gräve (1986), (8) Sramek (1975), (9) Israel & van der Hulst (1983), (10) Klein et al. (1996).

5.2.3 Spectral index

We had at our disposal again five usable maps of NGC 4449 - our new map at 350 MHz, the map at 610 MHz from Klein et al. (1996), NVSS map at 1.4 GHz from the archives and two maps at 4.9 GHz and 8.5 GHz from Chyży et al. (2000). All these maps were smoothed to the lowest resolution among all the five maps ($50\farcs11 \times 45\farcs00$). The H$\alpha$ map from Bomans et al. (1997) was scaled to the thermal flux density from the fit in Figure 5.9, in the same way as done for NGC 1569.

A spectral index map (Figure 5.10) between the three lowest frequencies was obtained. The core shows a flat spectra of around -0.4 as in NGC 1569. The spectra steepen into the halo to -0.7, but thereafter unexpectedly flattens in a patch in the western and southern sides (discussed in Sec. 6.1).

5.2.4 Radial evolution of the break

For NGC 4449, the width of each bin was taken as $50''$, since the beam size here is larger. The details of the error-analysis of each map can be found in Appendix A. The radial evolution of the break is shown in Figure 5.11. We again see the break migrating towards lower frequencies with time, but due to the peculiar spectral index behaviour, we see an anomalous rise in the break frequency at $200''$ and $250''$ radii. This area of the spectra (green patch in Figure 5.12) is doubtful.

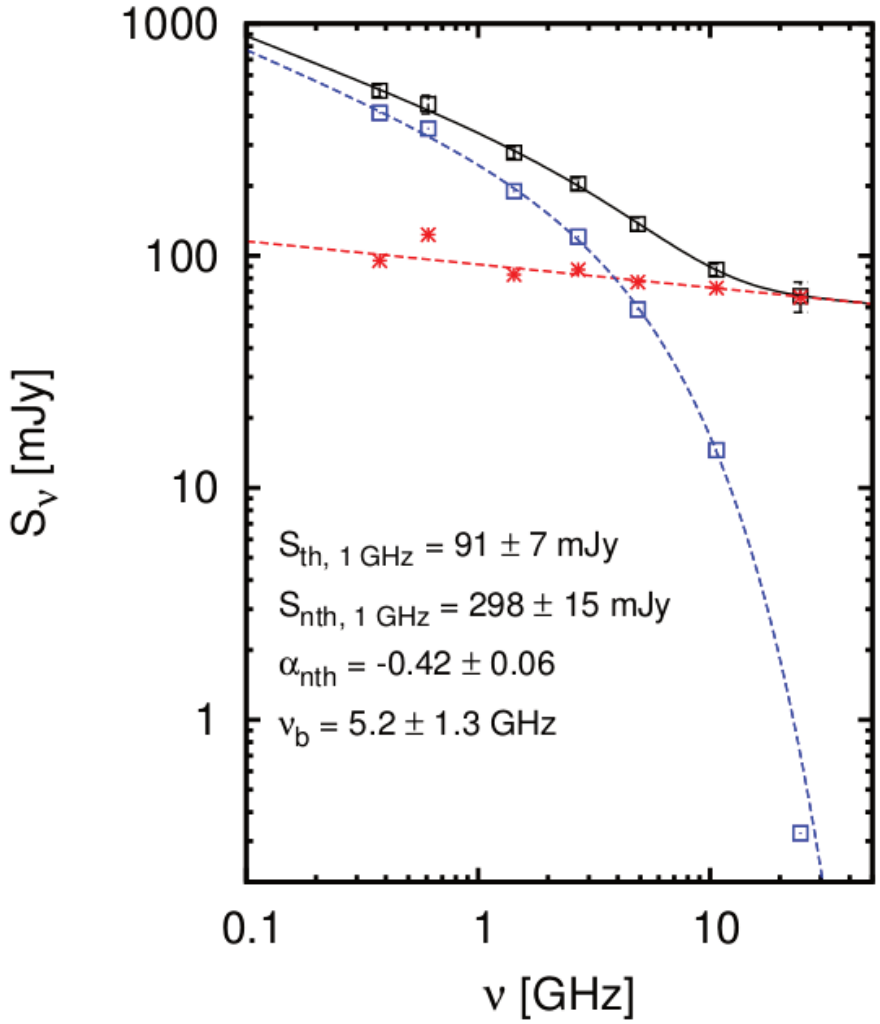

Fig. 5.9: Integrated radio continuum spectrum of NGC 4449, with the fitted total average flux densities (red squares), the free-free radiation (green crosses), and the synchrotron fluxes (blue stars), the latter obtained by subtracting the thermal from the total fluxes.

5.2.5 Equipartition magnetic field strength

We calculate the equipartition magnetic field strength, using exactly the same assumptions as for NGC 1569. The map resulting from our computations is shown in Figure 5.13. Average equipartition magnetic field strength over the whole galaxy turns out to be $\approx 10\,\mu$G, the same value as NGC 1569. The average value at the core is $\approx 17\,\mu$G, which is lower than that at the core of NGC 1569 corresponding to the lower radio emission. The average value in the halo is $\approx 9\,\mu$G, comparable to NGC 1569.

5.2.6 Spectral ages and wind velocity

To calculate the spectral ages using Eq. 5.2, we need to estimate the energy density of the radiation field, U_{rad}. We use the bolometric luminosity quoted in Karczewski et al.

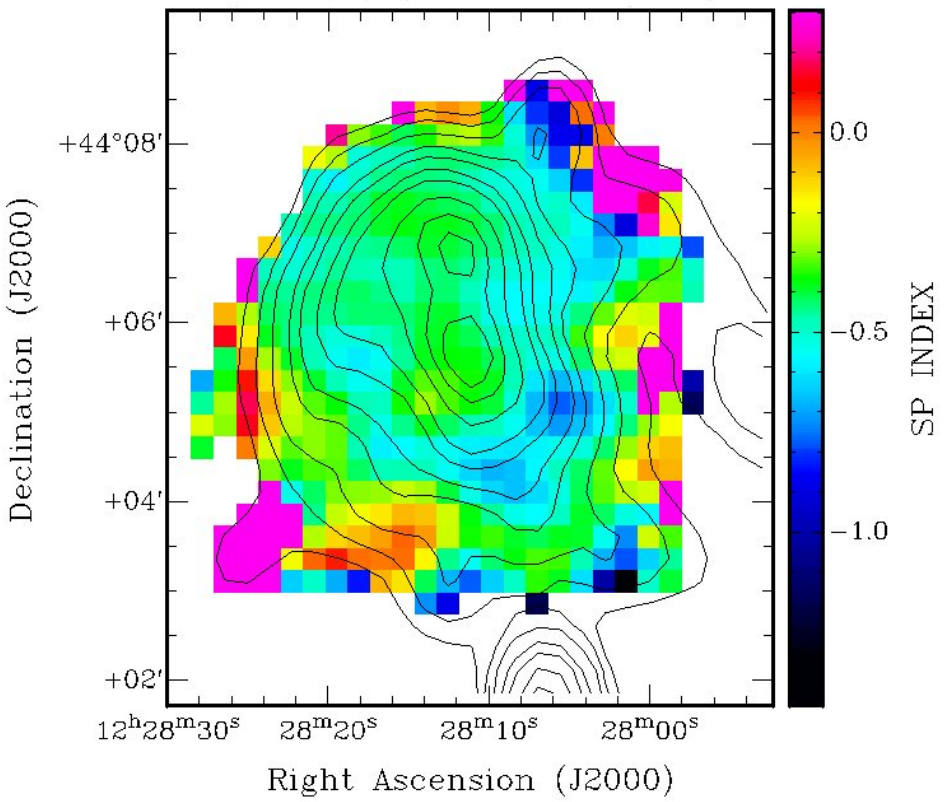

Fig. 5.10: Spectral index colour-map of NGC 4449 between 350 MHz, 610 MHz and 1.4 GHz. The colour-bar is in linear scale. Overlaid are the contours of the total power map at 350 MHz, same as in Fig. 5.8.

(2013) (discussed in Sec. 2.2):

$$L_{bol} = 5.7 \times 10^9 \, L_\odot = 2.188 \times 10^{36} \, \mathrm{W}. \tag{5.3}$$

Assuming that the radiating matter is distributed spherically, as in Lisenfeld et al. (2004):

$$U_{rad} = \frac{L_{bol}}{c\pi R^2} = \frac{(L_{bol}/\mathrm{W})}{(R/\mathrm{kpc})^2} \times 1.4 \times 10^{-35} \left[\frac{\mathrm{eV}}{\mathrm{cm}^3}\right], \tag{5.4}$$

where R is the radius of the sphere, and can be calculated using the average of the optical major and minor axes of 6.2 and 4.4 arcmin to be 3.1 kpc. Hence, we derive:

$$U_{rad} \equiv 3.2 \, \mathrm{eV \, cm^{-3}}. \tag{5.5}$$

Figure 5.14 shows the radial profile of the spectral ages of NGC 4449. From the linear fit, a wind velocity of $\approx 987 \pm 208 \, \mathrm{km \, s^{-1}}$ is calculated, which is also three times the escape velocity of $300 \, \mathrm{km \, s^{-1}}$ (Heckman et al., 1995; della Ceca et al., 1997). We note

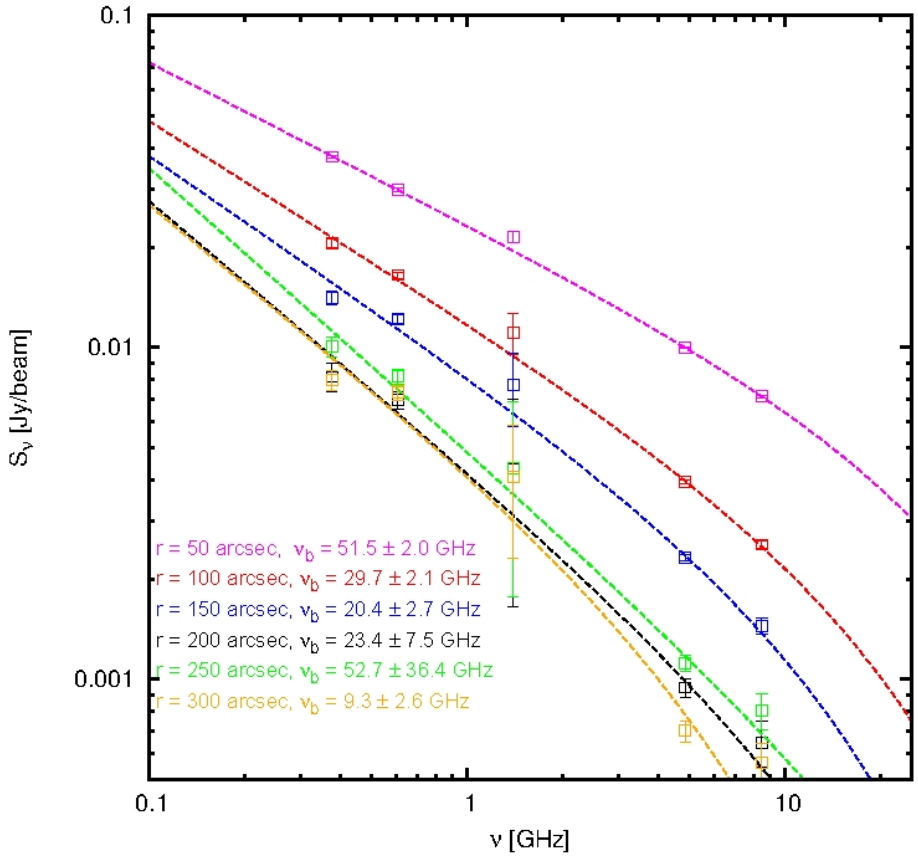

Fig. 5.11: Migration of the break frequency of NGC 4449 towards lower values with increasing radius.

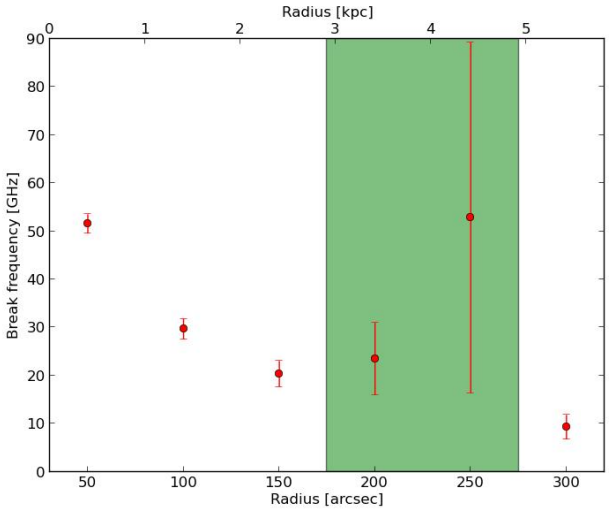

Fig. 5.12: NGC 4449: Plot of break frequency with errors against radius. The green patch indicates that the values of break frequency in this region are doubtful.

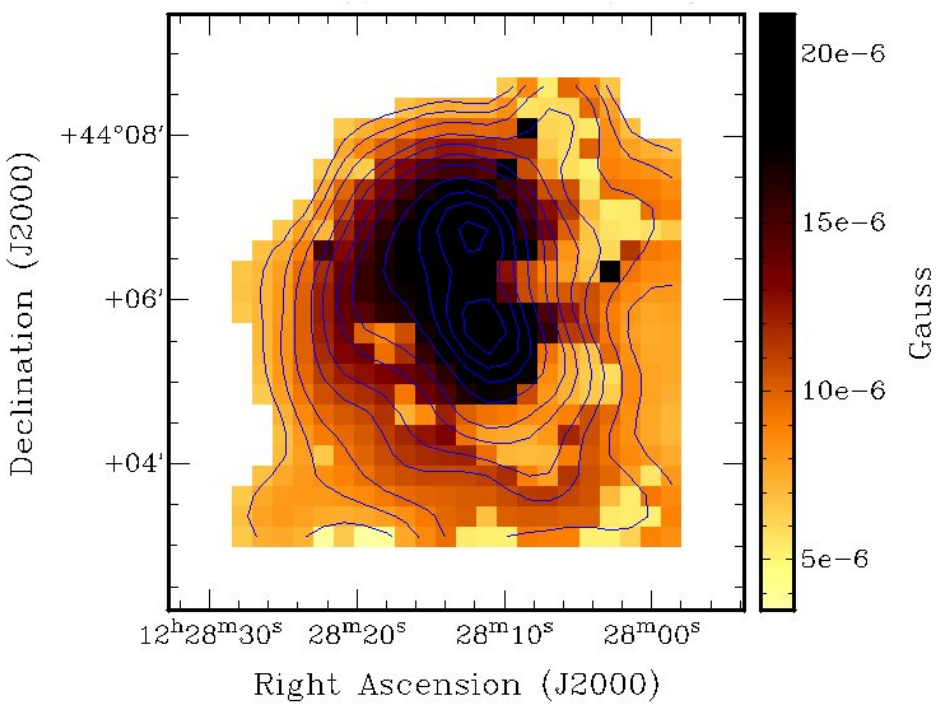

Fig. 5.13: Colour image of the total equipartition magnetic field strength estimated in NGC 4449. The colour-bar is linear. Overlaid are the contours of the non-thermal intensity at $\lambda 92\,\mathrm{cm}$.

that the estimated wind velocity for NGC 4449 is about a factor of three higher than that of NGC 1569. Table 5.4 summarises the main results of our analysis of NGC 4449.

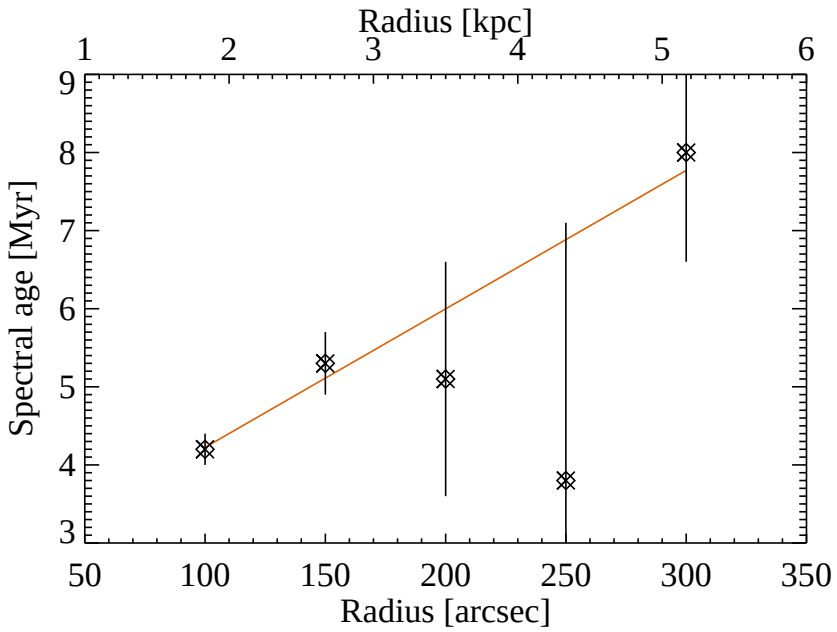

Fig. 5.14: NGC 4449: Plot of the estimated spectral ages with errors against radius. The fit is linear and the wind velocity is estimated from the slope.

r (arcsec)	r (kpc)	I_ν (Jy/beam)	α_{nth} -	ν_b (GHz)	B_{eq} (μG)	t_{spec} (Myr)
100	1.9	0.02061	-0.603 ± 0.0078	29.7 ± 2.1	8.5 ± 0.11	4.2 ± 0.2
150	2.9	0.01411	-0.654 ± 0.0203	20.4 ± 2.7	7.3 ± 0.11	5.3 ± 0.4
200	3.9	0.008161	-0.806 ± 0.0400	23.4 ± 7.5	6.1 ± 0.03	5.1 ± 1.5
250	4.8	0.01008	-0.850 ± 0.0377	52.8 ± 36.4	6.6 ± 0.04	3.8 ± 3.3
300	5.8	0.007983	-0.779 ± 0.0780	9.3 ± 2.5	6.2 ± 0.13	8.0 ± 1.4

Tab. 5.4: NGC 4449: Results at a glance - r is the galactocentric distance, I_ν is the intensity at $\lambda 92$ cm, α_{nth} is the non-thermal spectral index, ν_b is the break frequency, B_{eq} is the equipartition magnetic field strength and t_{spec} is the spectral age.

Chapter 6

Discussion, Conclusion & Future Prospects

6.1 Discussion

In this section, we discuss and interpret the results we had presented in Chap. 5. In Sec. 5.2.3, we had found that the spectral index map of NGC 4449 in Figure 5.10 showed an unexpected flattening in a particular patch in the halo. In order to further investigate the cause of this anomalous behaviour, we first looked at the radial distribution of intensity of the galaxy at all the frequencies. For this, we plotted the radially averaged intensities (Sec. 5.2.4), up to 3σ, of the non-thermal maps that were used to compute the spectral index map. The resulting plot in log-lin scale is shown in Figure 6.1, alongside the same plot made for NGC 1569.

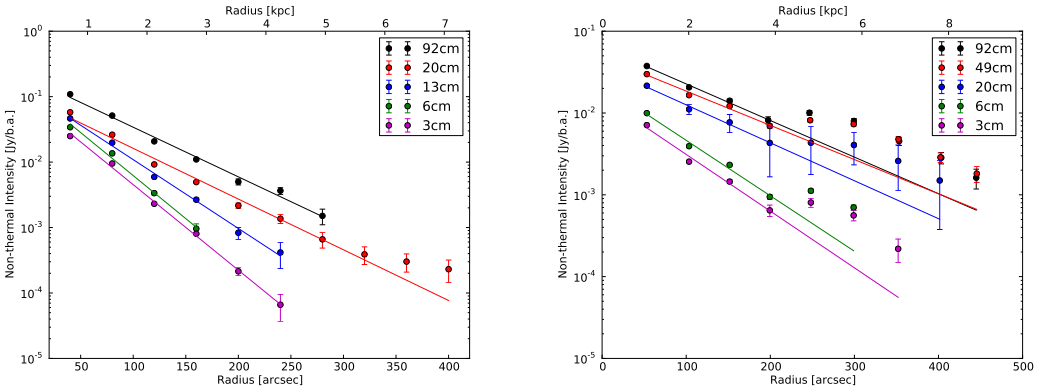

Fig. 6.1: Radial intensity distribution of NGC 1569 (left) and NGC 4449 (right) in log-lin scale.

The intensity of a galaxy usually decreases exponentially with increasing radius, which we see clearly for NGC 1569. However, for NGC 4449, there is a distinct increase in the average intensity at 250″ radius, for *all* the frequencies. This is indeed a surprising feature, and the radius coincides with the flat-spectra patch. Whether these two facts are correlated is hard to determine. One must keep in mind that the intensities have been radially averaged in elliptical rings of width 50″, and we cannot accurately determine which part of the ring at 250″ radius contributes to the increased intensity values. However, we can quantitatively measure the deviation of the intensities from

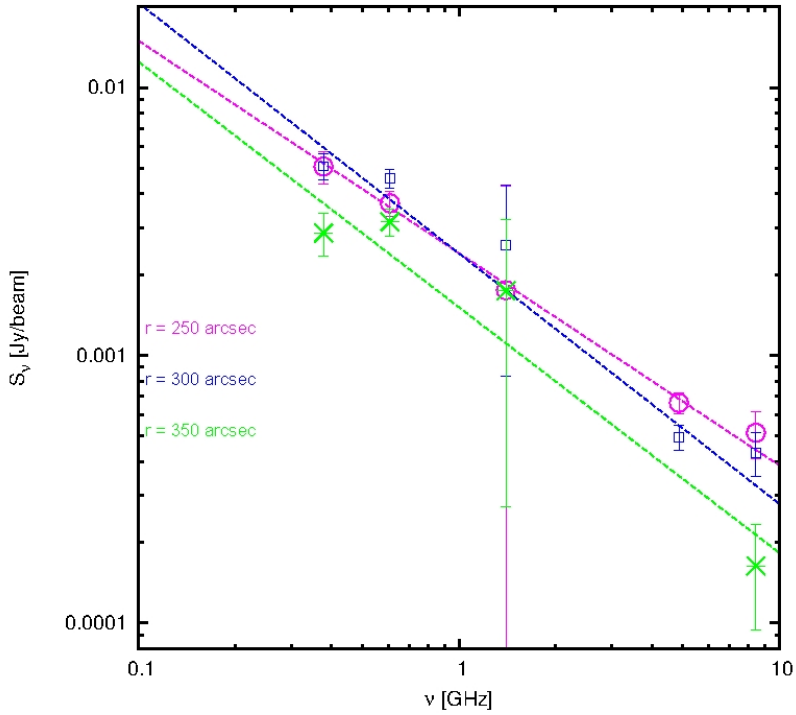

Fig. 6.2: Spectra of the "extra" flux in NGC 4449 are found to be non-thermal.

the exponential-fit (from Figure 6.1) for all the frequencies, and subsequently find the spectra of the "extra" flux at these radii. This can indicate if the spectrum flattens due to any thermal emission or not. The plot of the spectra of this "extra" flux in NGC 4449 is presented in Figure 6.2. The spectral indices from the power-law fits are found to lie between -0.7 and -0.9. Hence, the spectrum is essentially non-thermal and any possibility of thermal contamination can be ruled out.

We are still left with the question of why there is the spectral flattening. We rule out the possibility of multiple star-forming epochs having caused this intensity rise because Annibali et al. (2008) point out in their work that the star-formation of NGC 4449 has been mostly continuous over the last 1 Gyr (Sec. 2.2). If the spectral flattening happens to be real, then the break frequencies and the ages calculated are also possibly true within the errors, and this means that the cosmic-ray electrons in the halo of NGC 4449 are reaccelerated by turbulence or injected by shocks. We had discussed in Sec. 2.2, the X-ray study of Summers et al. (2003) which gave indications of an expanding superbubble of hot gas in the galaxy. The interaction of this superbubble with the colder gaseous halo might generate shocks and turbulence, which boost the radio luminosity in the halo and reaccelerate the cosmic-ray electrons.

In order to map the break frequency and do this whole analysis more accurately, it is clear that more sensitive high-frequency data for both galaxies are required. Observations with the VLA in the Ku band (12 - 18 GHz), K band (18 - 26.5 GHz) and Ka band (26.5 - 40 GHz) would fill the gaps in the high-energy part of the spectra (Figure 5.4 and 5.11). This would enable us to get a better fit to the model and estimate the spectral ages and hence the wind velocity more accurately.

The spectral indices at the core of both the galaxies are found to be flatter than -0.5 (Sec. 5.1.3 and Sec. 5.2.3), which is not in line with the standard first-order *diffusive shock acceleration* (Axford et al., 1977; Krymskii, 1977; Bell, 1978a,b; Blandford & Ostriker, 1978). This model does not take into account the effects of the magnetic field on the shocks. Lot of numerical studies, therefore, have been conducted to understand how the standard model is modified when a shock with high Mach number runs through a medium with a pre-existing population of cosmic-rays and magnetic fields. The resulting new model, which is more realistic, is called *non-linear diffusive shock acceleration* and gives the possibility of a flatter particle energy spectrum (Blasi, 2002; Amato & Blasi, 2005, 2006). This model is in line with recent observations of in supernova-remnants, with gamma-ray telescopes *Fermi* LAT (Giordano & Fermi LAT Collaboration, 2011) and VERITAS (Acciari et al., 2011).

We now discuss in some detail the primary question of this work: could starburst dwarf galaxies in the early universe have magnetised the inter-galactic medium (IGM)? The standard cosmological model tells us that structures in the universe formed in a bottom-up hierarchical manner, wherein small structures formed first and subsequently merged to form larger structures. With this idea in mind, stars are among the first objects in the universe. If one assumes that the magnetic fields were first seeded by battery effects within protogalactic gas clouds (where the first stars formed) in the early universe, then the process of subsequent galactic evolution can explain how starburst dwarfs can amplify these seed fields and drive them out along with their winds to extra-galactic scales. To test this theory, Beck et al. (2013a) presented a numerical model for the seeding and evolution of magnetic fields in protogalaxies. They showed a schematic overview of the magnetic build-up scenario during galaxy formation (Figure 6.3). Magnetic seed fields generated in the newly forming stars (O or B type) are amplified by dynamo action. When the stars explode as supernovae, their magnetic fields are carried with the gas to the interstellar medium. Here, a variety of processes can be responsible for further amplification of the magnetic fields (e.g. gravitational compression, turbulence and dynamo action). Additionally galactic merger events can contribute to the amplification of the magnetic field (Kotarba et al., 2011; Geng et al., 2012). Once the galactic halo virialises, μG-scale interstellar fields are produced. These fields are transported to the IGM by galactic outflows caused by supernovae-driven winds or galactic mergers mentioned above. The magnetic fields in the IGM can further be amplified by merger-induced shock waves, and possible dynamo action. The final magnetic field strength in their simulation reaches $\approx 10^{-3}\,\mu$G at the outskirts of the halo (IGM), at a scale > 100 kpc. It must be noted that various other seeding mechanisms exist - e.g. primordial (globally) and active galactic nuclei (locally).

Dubois & Teyssier (2010) had earlier numerically modelled the supernovae-driven winds in dwarf galaxies. Their simulations, along with the semi-analytical model of Bertone et al. (2006) and the simulations of Donnert et al. (2009) provided an understanding of the origin of an IGM magnetic field at a level of $10^{-4}\,\mu$G, assuming equipartition magnetic fields in dwarf galaxies (Figure 6.4).

The observed equipartition magnetic field strengths in our work are of the order of a few μG at the edge of the halos for both galaxies, which is of the same order of magnitude as that simulated by Beck et al. (2013a), but for larger Milky Way-like protogalaxies. The wind velocity of NGC 1569 estimated from our analysis is $\approx 255 \pm 12\,\mathrm{km\,s^{-1}}$ (Sec.

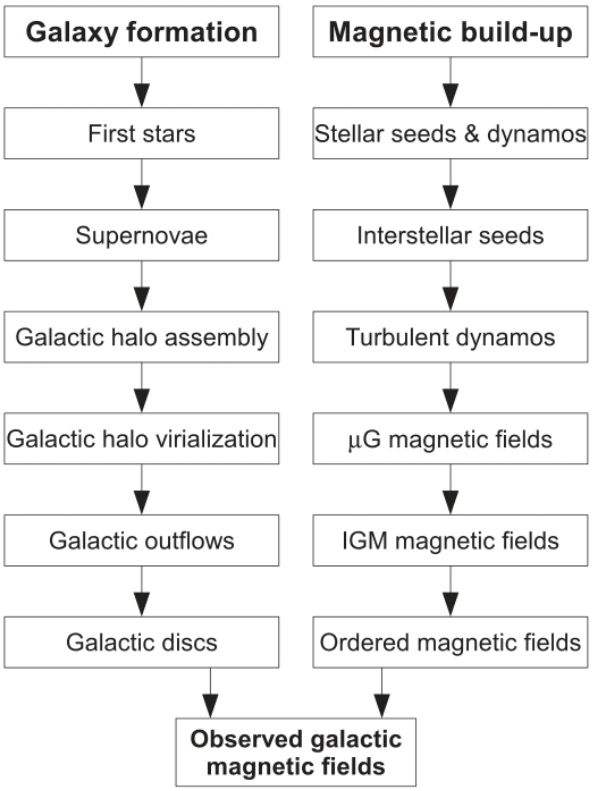

Fig. 6.3: Schematic overview of the process of supernovae magnetic seeding, amplification and ordering during structure formation. Taken from Beck et al. (2013a).

5.1.6). With this velocity, in one Gyr time, the wind will drive the magnetic fields and the cosmic ray electrons out of the galaxy to 260 kpc, and as a result, easily magnetise the inter-galactic medium. Moreover, if we assume the wind to be expanding like a spherical bubble which conserves magnetic energy, the magnetic field of 4 μG that we detect at ~ 5 kpc would reduce to $\approx 10^{-8}$ G at 260 kpc, which is comparable to IGM magnetic fields predicted by Beck et al. (2013a). For NGC 4449, if the anomaly in the spectra discussed above is not real, the resulting wind velocity within the errors also turns out to be three times the escape velocity and hence we can use the same argument as with NGC 1569.

We can therefore conjecture that if the synchrotron halos around the dwarf galaxies are observed to be larger, field strengths in the halo outskirts closer to the expected IGM values can be detected. Hence, we can predict that observations at even lower radio frequencies, using sensitive new telescopes (refer to Sec. 6.3), could possibly give a final answer to our question.

Galactic winds have been observed before in star-forming galaxies at all redshifts using spectroscopic data in high-energy (non-radio) regimes. They have been found to have wind velocities in the $100-500\,\mathrm{km\,s^{-1}}$ range (Heckman, 2000; Martin, 2005; Rubin et al., 2010). These works have attributed the winds to the stellar processes (described above). Outflows with significantly higher velocities ($> 1000\,\mathrm{km\,s^{-1}}$) were discovered by Tremonti et al. (2007) in a sample of massive ($\approx 10^{11} M_{\odot}$) post-starburst galaxies and it was

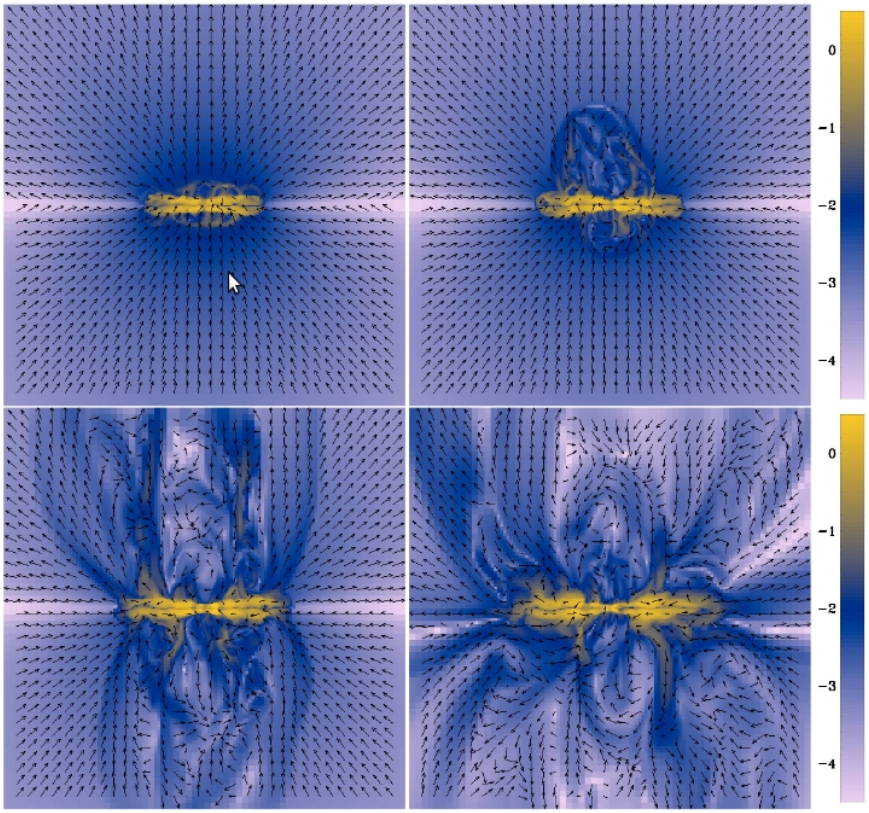

Fig. 6.4: Magnetic field in log μG units at different epochs t = 1 Gyr (upper left), t = 1.5 Gyr (upper right), t = 2 Gyr (bottom left) and t = 3 Gyr (bottom right). The image size is 40 kpc. Taken from Dubois & Teyssier (2010).

suggested that a more energetic source, such as feedback from an accreting supermassive black hole, may be responsible for launching the winds. However, Heckman et al. (2011); Diamond-Stanic et al. (2012) have recently proposed that feedback associated with a compact starburst is sufficient to produce the high-velocity outflows ($> 1000\,\mathrm{km\,s^{-1}}$) observed in massive galaxies, without the need to invoke feedback from an active galactic nucleus.

6.2 Conclusion

We conducted observations of starburst dwarf galaxies NGC 1569 and NGC 4449 at 350 MHz ($\lambda 92$ cm) with the WSRT. This is the first time dwarf galaxies have been observed at this frequency, and hence these observations provide an important bridge between future LOFAR observations and existing higher frequency observations. We found that the synchrotron halo of NGC 1569 is larger than previously seen at $\lambda 20$ cm, as expected. However, the synchrotron halo of NGC 4449 is the same size as that seen earlier at $\lambda 49$ cm.

The spectral indices in the core of both the galaxies are ~ -0.4. Such flat spectra at the core are observed in a dwarf galaxy for the first time. This might point towards

non-linear diffusive shock acceleration. The spectrum of NGC 4449 steepens into the halo to -0.7, but thereafter unexpectedly flattens in a patch in the western and southern sides, which, if real, can be due to reacceleration of electrons by turbulence or due to injection by shock.

Break in the radio spectrum radially migrates towards lower frequencies for NGC 1569 because of *electron cooling* due to synchrotron and inverse Compton losses. In the case of NGC 4449, the peculiar spectral index behaviour leads to an anomalous rise in the break frequency at 200″ and 250″ radii. The average equipartition magnetic field strengths are over the whole galaxy is $\approx 10\,\mu$G for both the galaxies, but the core field strength in NGC 1569 is higher than in NGC 4449 corresponding to higher radio emission. The magnetic field strength in the halo outskirts reach down to $\approx 4\,\mu$G, which is consistent with predictions from simulations. Rotation measure synthesis performed on NGC 1569 was unable to detect polarised emission.

Finally, and most importantly, the wind velocities estimated from the spectral ages for both the galaxies are *high*, approximately three times the escape velocities. This indicates that magnetic fields and cosmic-ray electrons can be dragged far out of the galaxy along with the wind, into the IGM. *Hence, it is reasonable that starburst dwarfs have played an important role in magnetising the IGM.* We conjecture that it is the sensitivity of the telescope that limits our detection of polarised emission and nano-Gauss level magnetic fields.

6.3 Future Perspective: LOFAR & SKA

Over the past two decades, there has been a renewed interest in low frequency radio astronomy, and the ever-increasing scientific need for more sensitive radio telescopes finally led to breakthroughs in innovation and realisation of dreams: SKA and its pathfinder, LOFAR (Figure 6.5). ASTRON[1] initiated LOFAR as a new and innovative effort to force a breakthrough in sensitivity for astronomical observations at radio-frequencies below 250 MHz. It opens the window to the so far unexplored low-energy synchrotron radio waves, emitted by cosmic-ray electrons in weak magnetic fields. LOFAR's exceptionally wide bandwidth is very useful for the study of magnetic fields, mainly because studies of Faraday rotation have the best precision when the range of measured wavelength is wide (Beck, 2010). The magnetism key science project (MKSP) aims to investigate cosmic magnetic fields in a variety of astrophysical sources, including an initial target list of galaxies, followed by deep observations of galaxies and galaxy groups (Beck et al., 2013b).

The LOFAR survey will provide a 5σ flux limit of 0.20 mJy/beam at 120 MHz assuming 8 hour of integration, with a synthesized beam of 0.″41 for the longest baselines, sensitivity and resolution far better than any radio telescope ever (van Haarlem et al., 2013). LOFAR will easily detect low-frequency radio halos of dwarf galaxies located at ~ 100 megaparsec distances, and the extent of these radio halos are expected to be larger than 50 kiloparsecs. To this end, we have already submitted a LOFAR Cycle 1 proposal to observe NGC 4449 (PI: K. Chyży). It is even possible that LOFAR will directly detect magnetic fields in the filamentary intergalactic medium of the Cosmic

[1] http://www.astron.nl/

Fig. 6.5: Left: LOFAR 'superterp' in the Netherlands on which six LOFAR stations are housed (image credit: Top-Foto, Assen). Right: Potential SKA array station placement in Australia and New Zealand indicating the 5,500 km baseline (image credit: CSIRO).

Web. If so, it will provide powerful observational constraints on the origin of cosmic magnetism.

The SKA, it is said, will be so sensitive that it will be able to detect an airport radar on a planet 50 light years away. The main platform on which the SKA's studies of cosmic magnetism will be based will be an All-Sky SKA Rotation Measure Survey, in which a year of observing time will yield Faraday rotation measures (RMs) for compact polarized extragalactic sources, an increase by five orders of magnitude over current data sets, and by three orders of magnitude over what could be accomplished with the VLA (Gaensler et al., 2004; Gaensler, 2009).

Appendix A

Error Analysis

As mentioned in Sec 5.1.4, we did an exhaustive error-analysis, to find the error in the intensities in all the total non-thermal intensity maps. The RMS in 5-7 different off-source regions in the map were read and the mean of that, σ_{noise}, was calculated. Additionally, the mean intensity in the same regions were also read and the standard deviation of the mean intensities, σ_{base}, was calculated. The error in the intensities in each ring was then given by:

$$\sigma_{total} = \frac{1}{\sqrt{N}} \cdot \sigma_{noise} + N \cdot \sigma_{base}, \tag{A.1}$$

where N is the number of beams in each bin. Since σ_{noise} is a statistical error and σ_{base} is a systematic error, they are added linearly.

We present below, for both the galaxies, the calculations, for each map, of σ_{noise} and σ_{base} in the first table, and the radially averaged non-thermal intensities with errors in the second table.

A.1 NGC 1569

λ92 cm:

Region	RMS [10^{-3}Jy/b.a.]	Mean [10^{-3}Jy/b.a.]
A	0.346	0.034
B	0.370	-0.089
C	0.363	-0.053
D	0.382	-0.113
E	0.368	-0.042
F	0.340	-0.109
G	0.363	-0.111

Tab. A.1: NGC 1569 at λ92 cm: RMS and Mean in different off-source regions of the map.

Therefore, $\sigma_{\text{noise}} = \langle \text{RMS} \rangle = 0.361$ mJy/b.a.
Average of the mean $= -0.069$ mJy/b.a.
$\sigma_{\text{base}} = 0.054$ mJy/b.a.

Ring	Inner [arcsec]	Outer [arcsec]	Points $\neq 0$	Average [10^{-3} Jy/beam]	Error [10^{-3} Jy / beam]	No. of Beams
1	20.0	60.0	20	108.79	0.362	2.28
2	60.0	100.0	38	51.36	0.408	4.34
3	100.0	140.0	58	20.74	0.498	6.62
4	140.0	180.0	54	10.99	0.479	6.17
5	180.0	220.0	64	5.00	0.528	7.31
6	220.0	260.0	52	3.65	0.469	5.94
7	260.0	300.0	37	1.51	0.404	4.22

Tab. A.2: NGC 1569 at λ92 cm: Radially averaged non-thermal intensities with calculated errors.

$\underline{\lambda 20\,\text{cm}}$:

Region	RMS [10^{-3}Jy/b.a.]	Mean [10^{-3}Jy/b.a.]
A	0.0545	-0.0221
B	0.0547	-0.0785
C	0.0784	-0.0144
D	0.0520	-0.0409
E	0.0737	-0.0416
F	0.0728	-0.0441

Tab. A.3: NGC 1569 at $\lambda 20\,\text{cm}$: RMS and Mean in different off-source regions of the map.

Therefore, $\sigma_{\text{noise}} = \langle \text{RMS} \rangle = 0.0643\,\text{mJy/b.a.}$
Average of the mean $= -0.0403$ mJy/b.a.
$\sigma_{\text{base}} = 0.0223$ mJy/b.a.

Ring	Inner [arcsec]	Outer [arcsec]	Points $\neq 0$	Average [10^{-3} Jy/beam]	Error [10^{-3} Jy / beam]	No. of Beams
1	20.0	60.0	20	57.68	0.0934	2.28
2	60.0	100.0	38	26.21	0.1276	4.34
3	100.0	140.0	64	9.21	0.1868	7.31
4	140.0	180.0	57	4.95	0.1704	6.51
5	180.0	220.0	71	2.17	0.2034	8.11
6	220.0	260.0	74	1.36	0.2106	8.45
7	260.0	300.0	59	0.66	0.1751	6.74
8	300.0	340.0	33	0.39	0.1172	3.77
9	340.0	380.0	20	0.30	0.0934	2.28
10	380.0	420.0	15	0.23	0.0873	1.71

Tab. A.4: NGC 1569 at $\lambda 20\,\text{cm}$: Radially averaged non-thermal intensities with calculated errors.

$\underline{\lambda 13\,\mathrm{cm}}$:

Region	RMS [10^{-3}Jy/b.a.]	Mean [10^{-3}Jy/b.a.]
A	0.07881	-0.05314
B	0.07583	-0.01153
C	0.07913	-0.01189
D	0.08783	-0.01602
D	0.08814	-0.01370
D	0.07962	-0.04021

Tab. A.5: NGC 1569 at $\lambda 13\,\mathrm{cm}$: RMS and Mean in different off-source regions of the map.

Therefore, $\sigma_{\mathrm{noise}} = \langle \mathrm{RMS} \rangle = 0.08156\,\mathrm{mJy/b.a.}$
Average of the mean $= -0.02442$ mJy/b.a.
$\sigma_{\mathrm{base}} = 0.01779$ mJy/b.a.

Ring	Inner [arcsec]	Outer [arcsec]	Points $\neq 0$	Average [10^{-3} Jy/beam]	Error [10^{-3} Jy / beam]	No. of Beams
1	20.0	60.0	20	46.44	0.09458	2.28
2	60.0	100.0	38	19.82	0.11636	4.34
3	100.0	140.0	64	5.93	0.16021	7.31
4	140.0	180.0	57	2.66	0.14778	6.51
5	180.0	220.0	71	0.83	0.17291	8.11
6	220.0	260.0	74	0.42	0.17838	8.45

Tab. A.6: NGC 1569 at $\lambda 13\,\mathrm{cm}$: Radially averaged non-thermal intensities with calculated errors.

$\underline{\lambda 6\,\text{cm}}$:

Region	RMS [10^{-3}Jy/b.a.]	Mean [10^{-3}Jy/b.a.]
A	0.07273	0.001022
B	0.06656	0.007517
C	0.05014	0.02902
D	0.04454	-0.03800
E	0.08385	-0.005573
F	0.04991	-0.02154

Tab. A.7: NGC 1569 at $\lambda 6\,\text{cm}$: RMS and Mean in different off-source regions of the map.

Therefore, $\sigma_{\text{noise}} = \langle \text{RMS} \rangle = 0.06129\,\text{mJy/b.a.}$
Average of the mean = 0.00259 mJy/b.a.
$\sigma_{\text{base}} = 0.02366$ mJy/b.a.

Ring	Inner [arcsec]	Outer [arcsec]	Points $\neq 0$	Average [10^{-3} Jy/beam]	Error [10^{-3} Jy / beam]	No. of Beams
1	20.0	60.0	20	34.07	0.09454	2.28
2	60.0	100.0	38	13.61	0.13210	4.34
3	100.0	140.0	64	3.36	0.19562	7.31
4	140.0	180.0	57	0.96	0.17805	6.51

Tab. A.8: NGC 1569 at $\lambda 6\,\text{cm}$: Radially averaged non-thermal intensities with calculated errors.

$\underline{\lambda 3\,\mathrm{cm}}$:

Region	RMS [10^{-3}Jy/b.a.]	Mean [10^{-3}Jy/b.a.]
A	0.02253	-0.005281
B	0.01841	-0.0001954
C	0.03448	-0.005325
D	0.02238	-0.002718

Tab. A.9: NGC 1569 at $\lambda 3\,\mathrm{cm}$: RMS and Mean in different off-source regions of the map.

Therefore, $\sigma_{\mathrm{noise}} = \langle \mathrm{RMS} \rangle = 0.02445\,\mathrm{mJy/b.a.}$
Average of the mean $= -0.00338$ mJy/b.a.
$\sigma_{\mathrm{base}} = 0.00245$ mJy/b.a.

Ring	Inner [arcsec]	Outer [arcsec]	Points $\neq 0$	Average [10^{-3} Jy/beam]	Error [10^{-3} Jy / beam]	No. of Beams
1	20.0	60.0	20	24.98	0.02178	2.28
2	60.0	100.0	38	9.52	0.02237	4.34
3	100.0	140.0	64	2.31	0.02695	7.31
4	140.0	180.0	57	0.80	0.02553	6.51
5	180.0	220.0	71	0.21	0.02846	8.11
6	220.0	260.0	74	0.07	0.02911	8.45

Tab. A.10: NGC 1569 at $\lambda 3\,\mathrm{cm}$: Radially averaged non-thermal intensities with calculated errors.

A.2 NGC 4449

$\underline{\lambda 92\,\mathrm{cm}}$:

Region	RMS [10^{-3}Jy/b.a.]	Mean [10^{-5}Jy/b.a.]
A	0.4388	-8.793
B	0.4245	3.290
C	0.4074	4.685
D	0.3852	-9.950
E	0.3539	-14.27
F	0.4164	2.180
G	0.4127	0.2200

Tab. A.11: NGC 4449 at $\lambda 92\,\mathrm{cm}$: RMS and Mean in different off-source regions of the map.

Therefore, $\sigma_{\mathrm{noise}} = \langle \mathrm{RMS} \rangle = 0.4056\,\mathrm{mJy/b.a.}$
Average of the mean = -0.03234 mJy/b.a.
$\sigma_{\mathrm{base}} = 0.07575$ mJy/b.a.

Ring	Inner [arcsec]	Outer [arcsec]	Points $\neq 0$	Average [10^{-3} Jy/beam]	Error [10^{-3} Jy / beam]	No. of Beams
1	25.0	75.0	26	37.54	0.4482	2.59
2	75.0	125.0	56	20.61	0.5950	5.59
3	125.0	175.0	72	14.11	0.6952	7.18
4	175.0	225.0	92	8.161	0.8292	9.18
5	225.0	275.0	72	10.08	0.6952	7.18
6	275.0	325.0	52	7.983	0.5712	5.19
7	325.0	375.0	42	4.528	0.5155	4.19
8	375.0	425.0	27	2.838	0.4511	2.69
9	425.0	475.0	22	1.618	0.4401	2.20

Tab. A.12: NGC 4449 at $\lambda 92\,\mathrm{cm}$: Radially averaged non-thermal intensities with calculated errors.

$\underline{\lambda 49\,\mathrm{cm}}$:

Region	RMS [10^{-3}Jy/b.a.]	Mean [10^{-5}Jy/b.a.]
A	0.5333	0.9820
B	0.5462	1.931
C	0.5268	-1.540
D	0.5927	-2.217
E	0.5475	3.763

Tab. A.13: NGC 4449 at $\lambda 49\,\mathrm{cm}$: RMS and Mean in different off-source regions of the map.

Therefore, $\sigma_{\mathrm{noise}} = \langle \mathrm{RMS} \rangle = 0.5493\,\mathrm{mJy/b.a.}$
Average of the mean = 0.00584 mJy/b.a.
$\sigma_{\mathrm{base}} = 0.02472$ mJy/b.a.

Ring	Inner [arcsec]	Outer [arcsec]	Points $\neq 0$	Average [10^{-3} Jy/beam]	Error [10^{-3} Jy / beam]	No. of Beams
1	25.0	75.0	26	29.91	0.4053	2.59
2	75.0	125.0	56	16.53	0.3705	5 .59
3	125.0	175.0	72	12.17	0.3825	7.18
4	175.0	225.0	104	6.938	0.4271	10.38
5	225.0	275.0	85	8.165	0.3982	8.48
6	275.0	325.0	60	7.307	0.3725	5.99
7	325.0	375.0	49	4.778	0.3693	4.89
8	375.0	425.0	33	2.868	0.3842	3.29
9	425.0	475.0	28	1.813	0.3978	2.79

Tab. A.14: NGC 4449 at $\lambda 49\,\mathrm{cm}$: Radially averaged non-thermal intensities with calculated errors.

$\underline{\lambda 20\,\text{cm}}$:

Region	RMS [10^{-3}Jy/b.a.]	Mean [10^{-5}Jy/b.a.]
A	0.4031	-0.1121
B	0.4191	0.1510
C	0.4530	-0.4330
D	0.4645	-0.2098

Tab. A.15: NGC 4449 at $\lambda 20\,\text{cm}$: RMS and Mean in different off-source regions of the map.

Therefore, $\sigma_{\text{noise}} = \langle \text{RMS} \rangle = 0.43493\,\text{mJy/b.a.}$
Average of the mean $= -0.15097$ mJy/b.a.
$\sigma_{\text{base}} = 0.0242$ mJy/b.a.

Ring	Inner [arcsec]	Outer [arcsec]	Points $\neq 0$	Average [10^{-3} Jy/beam]	Error [10^{-3} Jy / beam]	No. of Beams
1	25.0	75.0	26	21.55	0.8970	2.59
2	75.0	125.0	56	11.11	1.5367	5.59
3	125.0	175.0	72	7.696	1.8999	7.18
4	175.0	225.0	104	4.307	2.6470	10.38
5	225.0	275.0	100	4.328	2.5528	9.98
6	275.0	325.0	65	4.064	1.7390	6.48
7	325.0	375.0	53	2.593	1.4693	5.29

Tab. A.16: NGC 4449 at $\lambda 20\,\text{cm}$: Radially averaged non-thermal intensities with calculated errors.

$\underline{\lambda 6\,\mathrm{cm}}$:

Region	RMS [10^{-3}Jy/b.a.]	Mean [10^{-5}Jy/b.a.]
A	0.05999	-0.9862
B	0.05382	-0.4761
C	0.05559	-0.3635
D	0.05244	-0.3706
E	0.05345	0.2539

Tab. A.17: NGC 4449 at $\lambda 6\,\mathrm{cm}$: RMS and Mean in different off-source regions of the map.

Therefore, $\sigma_{\mathrm{noise}} = \langle \mathrm{RMS} \rangle = 0.05506\,\mathrm{mJy/b.a.}$
Average of the mean = -0.00389 mJy/b.a.
$\sigma_{\mathrm{base}} = 0.00441$ mJy/b.a.

Ring	Inner [arcsec]	Outer [arcsec]	Points $\neq 0$	Average [10^{-3} Jy/beam]	Error [10^{-3} Jy / beam]	No. of Beams
1	25.0	75.0	26	9.969	0.0456	2.59
2	75.0	125.0	56	3.933	0.0479	5.59
3	125.0	175.0	72	0.2320	0.0522	7.18
4	175.0	225.0	104	0.9446	0.0623	10.38
5	225.0	275.0	100	1.120	0.0614	9.98
6	275.0	325.0	72	0.6996	0.0522	7.18
7	325.0	375.0	56	0.07742	0.0479	5.59

Tab. A.18: NGC 4449 at $\lambda 6\,\mathrm{cm}$: Radially averaged non-thermal intensities with calculated errors.

$\underline{\lambda 3\,\text{cm}}$:

Region	RMS [10^{-3}Jy/b.a.]	Mean [10^{-5}Jy/b.a.]
A	0.06083	9.655
B	0.03772	7.880
C	0.05064	8.537
D	0.06228	9.389
E	0.04671	9.922

Tab. A.19: NGC 4449 at $\lambda 3\,\text{cm}$: RMS and Mean in different off-source regions of the map.

Therefore, $\sigma_{\text{noise}} = \langle \text{RMS} \rangle = 0.05164\,\text{mJy/b.a.}$
Average of the mean $= -0.09077$ mJy/b.a.
$\sigma_{\text{base}} = 0.00847$ mJy/b.a.

Ring	Inner [arcsec]	Outer [arcsec]	Points $\neq 0$	Average [10^{-3} Jy/beam]	Error [10^{-3} Jy / beam]	No. of Beams
1	25.0	75.0	26	7.122	0.0540	2.59
2	75.0	125.0	56	2.543	0.0692	5.59
3	125.0	175.0	72	1.450	0.0801	7.18
4	175.0	225.0	104	0.6456	0.1039	10.38
5	225.0	275.0	100	0.8048	0.1009	9.98
6	275.0	325.0	72	0.5605	0.0801	7.18
7	325.0	375.0	56	0.2187	0.0692	5.59

Tab. A.20: NGC 4449 at $\lambda 3\,\text{cm}$: Radially averaged non-thermal intensities with calculated errors.

Bibliography

Acciari, V. A., Aliu, E., Arlen, T., et al. 2011, ApJ, 730, L20

Adebahr, B., Krause, M., Klein, U., et al. 2013, A&A, 555, A23

Amato, E. & Blasi, P. 2005, MNRAS, 364, L76

Amato, E. & Blasi, P. 2006, MNRAS, 371, 1251

Angeretti, L., Tosi, M., Greggio, L., et al. 2005, AJ, 129, 2203

Annibali, F., Aloisi, A., Mack, J., et al. 2008, AJ, 135, 1900

Axford, W. I., Leer, E., & Skadron, G. 1977, in International Cosmic Ray Conference, Vol. 11, International Cosmic Ray Conference, 132–137

Bajaja, E., Huchtmeier, W. K., & Klein, U. 1994, A&A, 285, 385

Battaner, E. & Lesch, H. 2000, ArXiv Astrophysics e-prints

Beck, A. M., Dolag, K., Lesch, H., & Kronberg, P. P. 2013a, ArXiv e-prints

Beck, A. M., Lesch, H., Dolag, K., et al. 2012, MNRAS, 422, 2152

Beck, R. 2010, in ISKAF2010 Science Meeting

Beck, R., Anderson, J., Heald, G., et al. 2013b, Astronomische Nachrichten, 334, 548

Beck, R. & Hoernes, P. 1996, Nature, 379, 47

Beck, R. & Krause, M. 2005, Astronomische Nachrichten, 326, 414

Becker, R. H., White, R. L., & Edwards, A. L. 1991, ApJS, 75, 1

Bell, A. R. 1978a, MNRAS, 182, 147

Bell, A. R. 1978b, MNRAS, 182, 443

Bertone, S., Vogt, C., & Enßlin, T. 2006, MNRAS, 370, 319

Blandford, R. D. & Ostriker, J. P. 1978, ApJ, 221, L29

Blasi, P. 2002, Astroparticle Physics, 16, 429

Blumenthal, G. R. & Gould, R. J. 1970, Reviews of Modern Physics, 42, 237

Bomans, D. J., Chu, Y.-H., & Hopp, U. 1997, AJ, 113, 1678

Böttner, C., Klein, U., & Heithausen, A. 2003, A&A, 408, 493

Brandenburg, A. & Subramanian, K. 2005, Phys. Rep., 417, 1

Brentjens, M. A. & de Bruyn, A. G. 2005, A&A, 441, 1217

Brown, S. & Rudnick, L. 2011, MNRAS, 412, 2

Burn, B. J. 1966, MNRAS, 133, 67

Chakrabarti, S. K., Rosner, R., & Vainshtein, S. I. 1994, Nature, 368, 434

Chyży, K. T., Beck, R., Kohle, S., Klein, U., & Urbanik, M. 2000, A&A, 355, 128

Condon, J. J. 1987, ApJS, 65, 485

de Bruyn, A. G. & Brentjens, M. A. 2005, A&A, 441, 931

de Gasperin, F., Orrú, E., & Murgia, M. 2012, A&A, 547, A56

de Vaucouleurs, G. 1977, in Evolution of Galaxies and Stellar Populations, ed. B. M. Tinsley & R. B. G. Larson, D. Campbell, 43

della Ceca, R., Griffiths, R. E., & Heckman, T. M. 1997, ApJ, 485, 581

della Ceca, R., Griffiths, R. E., Heckman, T. M., & MacKenty, J. W. 1996, ApJ, 469, 662

Devost, D., Roy, J.-R., & Drissen, L. 1997, ApJ, 482, 765

Diamond-Stanic, A. M., Moustakas, J., Tremonti, C. A., et al. 2012, ApJ, 755, L26

Dolag, K., Kachelriess, M., Ostapchenko, S., & Tomàs, R. 2011, ApJ, 727, L4

Donati, J.-F. & Landstreet, J. D. 2009, ARA&A, 47, 333

Donnert, J., Dolag, K., Lesch, H., & Müller, E. 2009, MNRAS, 392, 1008

Dubois, Y. & Teyssier, R. 2010, A&A, 523, A72

Durrer, R. & Neronov, A. 2013, A&A Rev., 21, 62

Fletcher, A., Beck, R., Shukurov, A., Berkhuijsen, E. M., & Horellou, C. 2011, MNRAS, 412, 2396

Gaensler, B. M. 2009, in IAU Symposium, Vol. 259, IAU Symposium, ed. K. G. Strassmeier, A. G. Kosovichev, & J. E. Beckman, 645–652

Gaensler, B. M., Beck, R., & Feretti, L. 2004, New Astronomy Reviews, 48, 1003

Gaensler, B. M., Dickey, J. M., McClure-Griffiths, N. M., et al. 2001, ApJ, 549, 959

Galliano, F., Madden, S. C., Jones, A. P., et al. 2003, A&A, 407, 159

Galliano, F., Madden, S. C., Tielens, A. G. G. M., Peeters, E., & Jones, A. P. 2008, ApJ, 679, 310

Geng, A., Kotarba, H., Bürzle, F., et al. 2012, MNRAS, 419, 3571

Gil de Paz, A., Boissier, S., Madore, B. F., et al. 2007, ApJS, 173, 185

Ginzburg, V. L. & Syrovatskii, S. I. 1965, ARA&A, 3, 297

Giordano, F. & Fermi LAT Collaboration. 2011, Nuclear Instruments and Methods in Physics Research A, 630, 163

Giovannini, G., Bonafede, A., Feretti, L., et al. 2009, A&A, 507, 1257

Gregory, P. C. & Condon, J. J. 1991, ApJS, 75, 1011

Grocholski, A. J., Aloisi, A., van der Marel, R. P., et al. 2008, ApJ, 686, L79

Grocholski, A. J., van der Marel, R. P., Aloisi, A., et al. 2012, AJ, 143, 117

Han, J. L., Manchester, R. N., Lyne, A. G., Qiao, G. J., & van Straten, W. 2006, ApJ, 642, 868

Heald, G. 2009, in IAU Symposium, Vol. 259, IAU Symposium, ed. K. G. Strassmeier, A. G. Kosovichev, & J. E. Beckman, 591–602

Heckman, T. 2000, in Chandra Proposal, 638

Heckman, T. M., Borthakur, S., Overzier, R., et al. 2011, ApJ, 730, 5

Heckman, T. M., Dahlem, M., Lehnert, M. D., et al. 1995, ApJ, 448, 98

Heiles, C. & Crutcher, R. 2005, in Lecture Notes in Physics, Berlin Springer Verlag, Vol. 664, Cosmic Magnetic Fields, ed. R. Wielebinski & R. Beck, 137

Heitler, W. 1954, Quantum theory of radiation

Howard, A. M. & Kulsrud, R. M. 1997, ApJ, 483, 648

Hummel, E. 1980, A&AS, 41, 151

Hunter, D. A. & Elmegreen, B. G. 2004, AJ, 128, 2170

Hunter, D. A., Rubin, V. C., Swaters, R. A., Sparke, L. S., & Levine, S. E. 2002, ApJ, 580, 194

Hunter, D. A., Wilcots, E. M., van Woerden, H., Gallagher, J. S., & Kohle, S. 1998, ApJ, 495, L47

Israel, F. P. 1988, A&A, 194, 24

Israel, F. P. & de Bruyn, A. G. 1988, A&A, 198, 109

Israel, F. P. & van der Hulst, J. M. 1983, AJ, 88, 1736

Israel, F. P. & van Driel, W. 1990, A&A, 236, 323

Jones, A. P., Tielens, A. G. G. M., & Hollenbach, D. J. 1996, ApJ, 469, 740

Karczewski, O. Ł., Barlow, M. J., Page, M. J., et al. 2013, MNRAS, 431, 2493

Kardashev, N. S. 1962, Soviet Ast., 6, 317

Kepley, A. A., Mühle, S., Everett, J., et al. 2010, ApJ, 712, 536

Klein, U. & Gräve, R. 1986, A&A, 161, 155

Klein, U., Hummel, E., Bomans, D. J., & Hopp, U. 1996, A&A, 313, 396

Kotarba, H., Lesch, H., Dolag, K., et al. 2011, MNRAS, 415, 3189

Kronberg, P. P., Lesch, H., & Hopp, U. 1999, ApJ, 511, 56

Krymskii, G. F. 1977, Akademiia Nauk SSSR Doklady, 234, 1306

Kulsrud, R. M. & Zweibel, E. G. 2008, Reports on Progress in Physics, 71, 046901

Larsen, S. S., Origlia, L., Brodie, J., & Gallagher, J. S. 2008, MNRAS, 383, 263

Lisenfeld, U., Israel, F. P., Stil, J. M., & Sievers, A. 2002, A&A, 382, 860

Lisenfeld, U., Wilding, T. W., Pooley, G. G., & Alexander, P. 2004, MNRAS, 349, 1335

Longair, M. S. 2011, High Energy Astrophysics

Madden, S. C., Galliano, F., Jones, A. P., & Sauvage, M. 2006, A&A, 446, 877

Madden, S. C., Rémy-Ruyer, A., Galametz, M., et al. 2013, PASP, 125, 600

Martin, C. L. 1998, ApJ, 506, 222

Martin, C. L. 1999, ApJ, 513, 156

Martin, C. L. 2005, ApJ, 621, 227

Martin, C. L., Kobulnicky, H. A., & Heckman, T. M. 2002, ApJ, 574, 663

McQuinn, K. B. W., Skillman, E. D., Cannon, J. M., et al. 2010, ApJ, 721, 297

Mühle, S., Klein, U., Wilcots, E. M., & Hüttenmeister, S. 2003, Astronomische Nachrichten Supplement, 324, 40

Offringa, A. R., de Bruyn, A. G., Biehl, M., et al. 2010, MNRAS, 405, 155

Onaka, T., Matsumoto, H., Sakon, I., & Kaneda, H. 2010, A&A, 514, A15

Pacholczyk, A. G. 1970, Radio astrophysics. Nonthermal processes in galactic and extragalactic sources

Pasquali, A., Bik, A., Zibetti, S., et al. 2011, AJ, 141, 132

Pfleiderer, J., Durst, C., & Gebler, K.-H. 1980, MNRAS, 192, 635

Piddington, J. H. 1964, MNRAS, 128, 345

Piddington, J. H. 1972, Cosmic Electrodynamics, 3, 129

Press, W. H. & Schechter, P. 1974, ApJ, 187, 425

Press, W. H., Teukolsky, S. A., Vetterling, W. T., & Flannery, B. P. 1992, Numerical recipes in FORTRAN. The art of scientific computing

Rees, M. J. 1987, QJRAS, 28, 197

Reich, P. & Reich, W. 1986, A&AS, 63, 205

Roming, P. W. A., Kennedy, T. E., Mason, K. O., et al. 2005, Space Sci. Rev., 120, 95

Rubin, K. H. R., Weiner, B. J., Koo, D. C., et al. 2010, ApJ, 719, 1503

Rybicki, G. B. & Lightman, A. P. 1986, Radiative Processes in Astrophysics

Ryś, A., Grocholski, A. J., van der Marel, R. P., Aloisi, A., & Annibali, F. 2011, A&A, 530, A23

Sheth, R. K., Mo, H. J., & Tormen, G. 2001, MNRAS, 323, 1

Sramek, R. 1975, AJ, 80, 771

Stil, J. M. & Israel, F. P. 2002, A&A, 392, 473

Strong, A. W., Moskalenko, I. V., & Reimer, O. 2000, ApJ, 537, 763

Sulentic, J. W. 1976, ApJS, 32, 171

Summers, L. K., Stevens, I. R., Strickland, D. K., & Heckman, T. M. 2003, MNRAS, 342, 690

Theis, C. & Kohle, S. 2001, A&A, 370, 365

Tokura, D., Onaka, T., Takahashi, H., et al. 2006, ApJ, 648, 355

Tremonti, C. A., Moustakas, J., & Diamond-Stanic, A. M. 2007, ApJ, 663, L77

Vallenari, A. & Bomans, D. J. 1996, A&A, 313, 713

van Haarlem, M. P., Wise, M. W., Gunst, A. W., et al. 2013, A&A, 556, A2

Weingartner, J. C. & Draine, B. T. 2001, ApJ, 548, 296

Widrow, L. M. 2002, Reviews of Modern Physics, 74, 775

Widrow, L. M., Ryu, D., Schleicher, D. R. G., et al. 2012, Space Sci. Rev., 166, 37

Willson, M. A. G. 1970, MNRAS, 151, 1

Xu, H., Li, H., Collins, D. C., Li, S., & Norman, M. L. 2010, ApJ, 725, 2152